

JGR Planets

RESEARCH ARTICLE

10.1029/2019JE006299

Special Section:

Investigations of Vera Rubin Ridge, Gale Crater

Key Points:

- Images from the *Curiosity* rover show the presence of dark-toned diagenetic features at Vera Rubin ridge
- ChemCam analyses of these features point toward an Fe-oxide composition, consistent with crystalline hematite
- Depletion of Fe and Mn in bleached halos around the Fe-oxide features indicates mobility of Fe and Mn during the later stages of diagenesis

Supporting Information:

- Supporting Information S1
- Figures S1–S2

Correspondence to:

J. L'Haridon,
jlharidon@esf.org

Citation:

L'Haridon, J., Mangold, N., Fraeman, A. A., Johnson, J. R., Cousin, A., Rapin, W., et al. (2020). Iron mobility during diagenesis at Vera Rubin ridge, Gale Crater, Mars. *Journal of Geophysical Research: Planets*, 125, e2019JE006299. <https://doi.org/10.1029/2019JE006299>

Received 29 NOV 2019

Accepted 8 AUG 2020

Accepted article online 28 AUG 2020

Author Contributions:

Conceptualization: J. L'Haridon, N. Mangold, A. A. Fraeman, J. R. Johnson, A. Cousin, W. Rapin, G. David, E. Dehouck, V. Sun, J. Frydenvang, O. Gasnault, P. Gasda, N. Lanza, O. Forni, P.-Y. Meslin, S. P. Schwenzer, J. Bridges, B. Horgan, C. H. House, M. Salvatore























Data curation: J. R. Johnson, A. Cousin, W. Rapin, G. David, O. Gasnault, O. Forni, P.-Y. Meslin

Formal analysis: J. L'Haridon

Investigation: J. L'Haridon, N. Mangold

(continued)

Iron Mobility During Diagenesis at Vera Rubin Ridge, Gale Crater, Mars

J. L'Haridon¹ , N. Mangold¹ , A. A. Fraeman² , J. R. Johnson³ , A. Cousin⁴ , W. Rapin⁵ , G. David⁴ , E. Dehouck⁶ , V. Sun² , J. Frydenvang⁷ , O. Gasnault⁴ , P. Gasda⁸ , N. Lanza⁸ , O. Forni⁴ , P.-Y. Meslin⁴ , S. P. Schwenzer⁹ , J. Bridges¹⁰ , B. Horgan¹¹ , C. H. House¹² , M. Salvatore¹³ , S. Maurice⁴ , and R. C. Wiens⁸ 

¹Laboratoire de Planétologie et Géodynamique, UMR6112, CNRS, Université de Nantes, Nantes, France, ²Jet Propulsion Laboratory, California Institute of Technology, Pasadena, CA, USA, ³Johns Hopkins University Applied Physics Laboratory, Laurel, MD, USA, ⁴IRAP, Univ. Toulouse, CNRS, CNES, Toulouse, France, ⁵Geological and Planetary Sciences, California Institute of Technology, Pasadena, CA, USA, ⁶Univ Lyon, Univ Lyon 1, ENSL, CNRS, LGL-TPE, F-69622, Villeurbanne, France, ⁷Globe Institute, University of Copenhagen, Copenhagen, Denmark, ⁸Los Alamos National Laboratory, Los Alamos, NM, USA, ⁹AstrobiologyOU, EEES, Open University, Milton Keynes, UK, ¹⁰School of Physics and Astronomy, University of Leicester, Leicester, UK, ¹¹Department of Earth, Atmospheric, and Planetary Sciences, Purdue University, West Lafayette, IN, USA, ¹²Department of Geosciences, Pennsylvania State University, State College, PA, USA, ¹³Department of Astronomy and Planetary Science, North Arizona University, Flagstaff, AZ, USA

Abstract The *Curiosity* rover investigated a topographic structure known as Vera Rubin ridge, associated with a hematite signature in orbital spectra. There, *Curiosity* encountered mudstones interpreted as lacustrine deposits, conformably overlying the 300 m-thick underlying sedimentary rocks of the Murray formation at the base of Mount Sharp. While the presence of hematite ($\alpha\text{-Fe}_2\text{O}_3$) was confirmed in situ by both Mastcam and ChemCam spectral observations and by the CheMin instrument, neither ChemCam nor APXS observed any significant increase in FeO_T (total iron oxide) abundances compared to the rest of the Murray formation. Instead, *Curiosity* discovered dark-toned diagenetic features displaying anomalously high FeO_T abundances, commonly observed in association with light-toned Ca-sulfate veins but also as crystal pseudomorphs in the host rock. These iron-rich diagenetic features are predominantly observed in “gray” outcrops on the upper part of the ridge, which lack the telltale ferric signature of other Vera Rubin ridge outcrops. Their composition is consistent with anhydrous Fe-oxide, as the enrichment in iron is not associated with enrichment in any other elements, nor with detections of volatiles. The lack of ferric absorption features in the ChemCam reflectance spectra and the hexagonal crystalline structure associated with dark-toned crystals points toward coarse “gray” hematite. In addition, the host rock adjacent to these features appears bleached and shows low- FeO_T content as well as depletion in Mn, indicating mobilization of these redox-sensitive elements during diagenesis. Thus, groundwater fluid circulations could account for the remobilization of iron and recrystallization as crystalline hematite during diagenesis on Vera Rubin ridge.

Plain Language Summary The NASA rover *Curiosity* investigated Vera Rubin ridge, a specific landform within the Gale crater on Mars. Scientific missions in orbit around the planet had previously discovered high concentrations of hematite on top of the ridge, an iron-oxide mineral that commonly forms in water. However, it was not clear from orbit if such conditions existed at the time of the deposition of the sediments (around 3.5 billion years ago) or occurred much later during “diagenesis,” after deposition of the sediments and up to their transformation into rocks. On the surface, the rover did not observe significant differences between the ridge and the terrains encountered before it, except for small, dark geologic features that formed during diagenesis. Their analysis by the ChemCam instrument revealed that these features are composed of hematite—the same iron-oxide mineral that was observed from orbit—and, interestingly, that the iron required to form them was removed from the adjacent rocks by groundwaters. As such, it appears that groundwaters played an important role in shaping Vera Rubin ridge, and thus partially obscure interpretations on the environmental conditions that existed on the surface of Mars at the time of sedimentation.

Methodology: J. L'Haridon, S. Maurice, R. C. Wiens

Project administration: A. A. Fraeman, S. Maurice, R. C. Wiens

Supervision: N. Mangold

Visualization: J. L'Haridon

Writing - original draft: J. L'Haridon, N. Mangold

Writing - review & editing: J. L'Haridon, N. Mangold

1. Introduction

In 2012, the Mars Science Laboratory (MSL) *Curiosity* rover landed on the plains of an ~155 km diameter impact crater, Gale crater, north of the 5 km-high sedimentary mound (Aeolis Mons, informally referred to as Mount Sharp) that sits at its center (Grotzinger et al., 2012). After 1,800 sols (sol = Martian day) and ~17 km of traverse across regolith and outcrops of fluvio-lacustrine deposits (Grotzinger et al., 2014, 2015; Vasavada et al., 2014) and of local remnant of a draping eolian unit (Banham et al., 2018), the rover reached Vera Rubin ridge (VRR), on the lower slopes of Mount Sharp (Figure 1). This ~6.5 km-long and ~200 m-wide topographic sedimentary feature trends northeast-southwest on the fringe of the phyllosilicate-bearing trough (Glen Torridon) and overlying sulfate deposits (Anderson, 2010; Fraeman et al., 2016; Milliken et al., 2010). It also displays higher thermal inertia and greater resistance to erosion compared to the adjacent terrains, from both orbital and in situ perspectives.

Hyperspectral observations from the Compact Reconnaissance Imaging Spectrometer for Mars (CRISM) instrument onboard Mars Reconnaissance Orbiter (MRO) revealed a distinctive crystalline hematite signature on the upper-most part of the ridge (Fraeman et al., 2013). The hematite-rich nature of the ridge was interpreted as evidence for the involvement of redox-driven processes (iron oxidation) in its formation, either related to primary deposition (e.g., redox interface in the lacustrine setting or soil formation) or post-depositional processes during diagenesis (e.g., oxidation by neutral to acidic groundwater) (Fraeman et al., 2013). VRR thus provides a unique opportunity to investigate redox processes on Mars but also to compare orbital observations and interpretations against the ground truth. As such, this topographic structure constitutes a key milestone in the rover's investigation of the Gale crater's geological history and its implications for past habitability on the planet (Fraeman et al., 2020).

The VRR rocks exhibit a range of geological features that formed during diagenesis, that is, after deposition of the sediments and through their burial and induration into sedimentary rocks. The pervasive light-toned Ca-sulfate veins encountered in all geological units crossed by the rover traverse so far (L'Haridon et al., 2018; Nachon et al., 2014; Rapin et al., 2016) are also abundant throughout VRR (Figure 1). In addition, crystal molds, nodules, and concretions are observed in close association with Ca-sulfate-filled veins. In this study, we report results from the ChemCam instrument with respect to small-scale diagenetic features observed at VRR. Lastly, we discuss the potential implications of these findings with respect to previous observations in Gale crater and argue for the significant role played by diagenetic processes in the formation of the VRR sedimentary rocks.

2. Methods

2.1. The ChemCam Instrument

The ChemCam instrument (Maurice et al., 2012; Wiens et al., 2012) consists of a Laser-Induced Breakdown Spectroscopy (LIBS) system associated with the Remote Micro-Imager (RMI) camera (Le Mouélic et al., 2015). The LIBS technique involves focusing a pulsed laser on the target material (located up to 7 m from the mast of the rover), which leads to the formation of a plasma. Elemental composition is derived from the analysis of the light emitted by the plasma by three spectrometers (covering the spectral ranges of 240–342, 382–469, and 474–906 nm), which resolve the emission peaks associated with the decay of its excited atoms, ions, and molecules to lower electronic states. ChemCam analyses comprise several closely spaced observation points, each typically composed of 30 laser shots on a given point. The first few laser shots remove the dust cover from the surface of the target, so the subsequent laser shots provide the composition of the dust-free surface targeted material.

ChemCam provides fine-scale chemical analyses especially suited to characterizing isolated geological features such as concretions, nodules, or fracture fills. Indeed, the ablated area is tiny, covering about 300 to 600 μm in diameter, and up to a few micrometers per laser shot in depth depending on the targeted material (Maurice et al., 2012), making ChemCam analyses complementary to the bulk analyses of the other instruments on the rover. While ChemCam was not designed to provide information on mineralogy, ChemCam chemical analyses on geological features of a size comparable to or larger than the ablated area can still be used to infer the associated mineral phases. Nonetheless, even at these scales, it is not unusual for ChemCam to analyze a mixture of compositions if the observation point is located at the interface

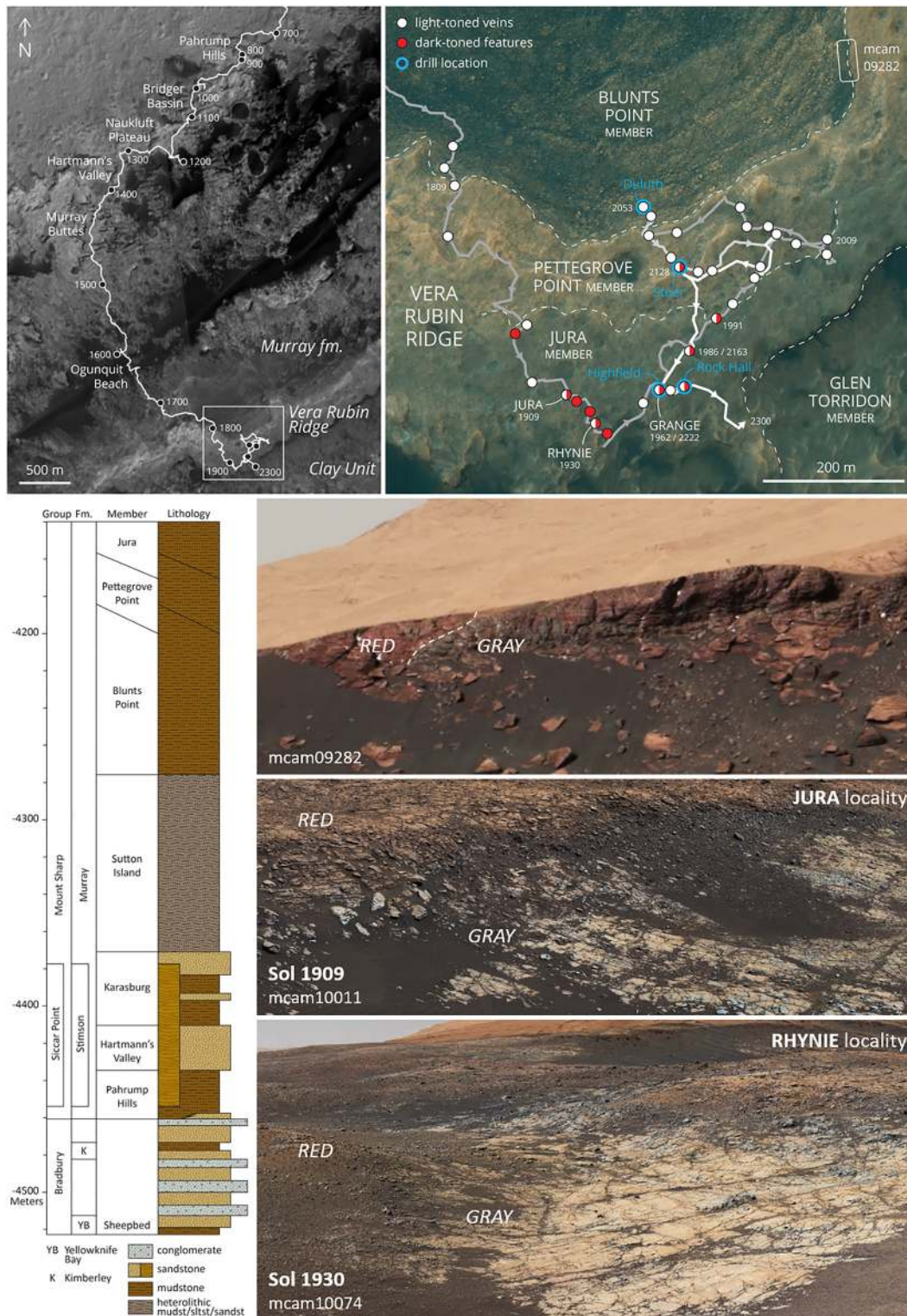


Figure 1. Location of Vera Rubin ridge along the rover traverse in Gale crater (top left) and a close-up view of the explored portion of the ridge displaying the location of ChemCam analyses of diagenetic features and of the drilling sites (top right). Stratigraphic column of the terrains explored by the rover (bottom left, adapted from Edgar et al., 2020), showing that VRR is composed of the Pettegrove Point and Jura members and that it is part of the Murray formation. Mastcam mosaics (bottom right) illustrating the lateral red and gray color variations in the bedrock on Vera Rubin ridge observed from a distance during the rover approach on the north flank of the ridge (mcam09282) and associated with topographic depressions, notably at the “Jura” (mcam10011), “Rhynie” (mcam10074), and “Highfield” localities.

between distinctive geological features. For instance, observation points on light-toned veins commonly show mixing between Ca-sulfate from the veins and the surrounding host rock composition (L'Haridon et al., 2018; Nachon et al., 2014, 2016; Rapin et al., 2016).

In addition to LIBS chemical analyses, the ChemCam spectrometers also acquire passive reflectance spectra (without active use of the laser) after each LIBS observation, thus recording the radiance of the targeted material in the visible/near-infrared (400–840 nm). The passive reflectance data can guide interpretations on mineralogy as it provides additional information on the presence of ferric (Fe^{3+} -bearing) mineral phases and their crystallinity, such as hematite (Johnson et al., 2015, 2016), which is not identifiable from LIBS analyses alone. The angular field of view of ~ 0.65 mrad of the spectrometer is wider than the ablation area of the LIBS, corresponding to a 2 mm diameter area on the surface at a distance of 3 m from the rover (50% of ChemCam targets are within 2 to 3 m from the rover and 45% within 3 to 5 m; Maurice et al., 2016).

2.2. Elemental Composition and Quantification

ChemCam detects and quantifies the abundances of most major elements as weight percent of oxides (SiO_2 , TiO_2 , Al_2O_3 , and total iron oxide expressed as FeO_T , MgO , CaO , Na_2O , and K_2O), using a combination of the “partial least squares” (PLS) and “independent component analysis” (ICA) multivariate analytical methods to provide the multivariate oxide composition (MOC) data set (Clegg et al., 2017). The quantification of major elements was later refined with the expansion from 66 to 408 standards for the ChemCam calibration database (Clegg et al., 2017; Wiens & Maurice, 2015). The accuracy of ChemCam measurements is estimated for each major element through the calculation of the root mean squared error of prediction (RMSEP) for a representative test set of standards. Since accuracy varies with elemental abundances, a submodel approach has been developed in order to provide more accurate abundances across the distinct compositional ranges observed for each element on Mars (Anderson et al., 2017; Clegg et al., 2017). The precision of ChemCam measurements is defined by the repeatability of point-to-point and the shot-to-shot prediction variations either on the target itself, selected homogeneous targets or the calibration targets (Clegg et al., 2017, and references therein).

ChemCam is also able to detect and quantify a number of minor and trace elements using a univariate method in which a single emission peak is calibrated for the abundance of that element: Mn (Lanza et al., 2014); Zn (Lasue et al., 2016); F (Forni et al., 2015); Sr, Li, Ba, and Rb (Payré et al., 2017); Cu (Payré et al., 2019); and B (Gasda et al., 2017). Furthermore, the H signal observed in the LIBS spectra can be used to determine the hydration state for specific compositions (Rapin et al., 2016). Finally, a few other volatile elements (such as S, P, and Cl) are only observed qualitatively but are often used for chemical and mineralogical diagnostic studies (Meslin et al., 2018; Nachon et al., 2016). Additional work is currently in progress to quantify these volatile elements systematically (Anderson et al., 2017; Clegg et al., 2018; Meslin et al., 2016; Rapin et al., 2019; Thomas et al., 2018).

High-Fe compositions are, however, still poorly represented in the current database (Clegg et al., 2017), with only two samples with >40 wt.% FeO_T , which notably leads to an underestimation of FeO_T in Fe-oxide-dominated compositions on Mars. Recent laboratory LIBS analyses of hematite-basalt mixtures and iron meteorite samples yielded improved predictions for FeO_T (David et al., 2020). While this laboratory work was not yet incorporated in the ChemCam quantification models at the time of writing, the data for FeO_T from David et al., 2020 will be used in this study to characterize the variability of FeO_T associated with diagenesis on VRR, especially for high- FeO_T abundances. Also, the abundances in FeO_T reported here corresponds to the total iron oxide content, as ChemCam is unable to distinguish native, ferrous, and ferric iron. This study includes the ChemCam data acquired from sols 1,809 to 2,300 (431 ChemCam targets and 3,554 individual points), covering the whole exploration of VRR. ChemCam observations on float rocks, meteorites, wind-blown sand, drill tailings, and drill material dump piles were not included in the data set of this study, as they do not contribute to the purpose of this study.

2.3. Mastcam and MAHLI Cameras

The VRR outcrops were documented by the Mast Cameras (Mastcam) and Mars Hand Lens Imager (MAHLI). The two Mastcam cameras (34 and 100 mm focal lengths), located on the mast, provide contextual color images for ChemCam observations at the outcrop scale, with a $150 \mu\text{m}/\text{pixel}$ resolution at 2 m (Malin et al., 2017). MAHLI, mounted on the robotic arm of the rover, provides high-resolution (up to $14 \mu\text{m}/\text{pixel}$ at

the minimum distance of 2.1 cm) color close-up images of outcrops that provide textural and structural information on fine-scale geological features, such as mineralized veins and concretions, as well as valuable mineralogical information regarding the shape, cleavage, color, fluorescence, and luster of individual mineral grains (Edgett et al., 2012). The analysis of crystal morphology was conducted on MAHLI images using the Fiji distribution (Schindelin et al., 2012) of the ImageJ open-source software (Abràmoff et al., 2004).

3. Geological Setting of VRR

3.1. Stratigraphy

The VRR structure was defined by its topographic prominence in orbital images. Following in situ observations, it was later divided into two members representing the lower and upper sections of the ridge (Edgar et al., 2020). The lower member, named Pettegrove Point, is composed of well-cemented and finely laminated mudstones crosscut by light-toned filled fractures. The upper member, Jura, conformably overlies Pettegrove Point and consists primarily of red blocky outcrops of finely laminated mudstone to fine-grained sandstones. The sedimentary facies and textures observed in both members of VRR are consistent with deposition in a lacustrine setting (Edgar et al., 2020). The lack of clear discontinuity between VRR and the underlying fluvial and lacustrine fine-grained sandstones and mudstones of the Murray formation suggests a continuity in the depositional environment. As such, VRR is regarded as a continuation of the Murray formation, which has been observed consistently along the rover traverse since sol ~750, when *Curiosity* reached the lowest strata of Mount Sharp at Pahrump Hills (encompassing >300 m in thickness) (Fedó et al., 2018; Grotzinger et al., 2015). We refer the reader to Edgar et al. (2020) for a detailed description of the sedimentology and sedimentary rock textures.

Both Pettegrove Point and Jura members also display lateral color variations in the form of meter- to decameter-scale patches of gray, fine-grained, laminated bedrock (Horgan et al., 2020), first noted on the flanks of VRR during the approach (Figure 1), and which do not appear to be stratigraphically controlled (Edgar et al., 2020; Fraeman et al., 2020). The gray outcrops are more prominently observed in the Jura member where they display less resistance to mechanical erosion compared to adjacent red blocky outcrops. These outcrops form bright patches in shallow topographic depressions on top of the ridge (Fraeman et al., 2020) and were notably explored at the Jura, Rhynie, and Highfield localities (Figure 1). Interestingly, the gray outcrops also appear to exhibit slightly coarser grain size compared to the adjacent red outcrops, based on the analysis of the variability of ChemCam shots (Bennett et al., 2020; Edgar et al., 2020). Nevertheless, since these lateral outcrop color and spectral variations crosscut the stratigraphy, they suggest a significant diagenetic overprinting on the formation of the ridge.

3.2. Chemical and Mineralogical Composition

Chemical analysis from the ChemCam and Alpha-Particle X-ray Spectrometer (APXS) instruments onboard *Curiosity* reports elemental bulk compositions for VRR bedrock within the compositional ranges of the Murray formation (Frydenvang et al., 2020; Thompson et al., 2020). The lack of enrichments in FeO_T compared to the underlying Murray sedimentary rocks indicates that the iron forming the hematite detected from orbital data did not come from an external source. Nevertheless, ChemCam and APXS both report modest chemical variations in major elements with slightly higher silica and aluminum contents than in the underlying Murray rocks, as well as local depletion in iron. Minor elements also vary, with much lower lithium overall and significant variations in manganese, which are not always correlated with variations in iron (David et al., 2020; Frydenvang et al., 2020; Thompson et al., 2020).

To further investigate this chemical variability, the *Curiosity* rover carried out three drilling campaigns on VRR—one in the Pettegrove Point member (Stoer or ST drill target) and two in the Jura member, within both red outcrops (Rock Hall or RH drill target) and gray outcrops (Highfield or HF drill target) (Figure 1). Through the mineralogical analysis of the drill samples, the CheMin instrument (X-ray diffractometer) shows that hematite is detected at all three drill sites, albeit in lower abundance within the red outcrops of the Jura member (Rampe et al., 2020) compared to the rest of VRR. Overall, the VRR drill samples contain more hematite compared to the Murray formation (Rampe et al., 2020). In situ Mastcam multispectral and ChemCam passive reflectance observations confirm that fine-grained red hematite is present

systematically in the red to purple VRR outcrops, likely alongside with nanophase hematite (Horgan et al., 2020). Indeed, brushed VRR bedrocks display ferric spectral features (535 nm band depth, 750 to 840 nm slope, 860 nm band depth) (Fraeman et al., 2018, 2019), with the exception of the gray outcrops of the Jura member that lack this ferric spectral signature (Horgan et al., 2020). This is interpreted to reflect a lack of fine-grained and nanophase hematite in the gray outcrops but may still be consistent with the presence of coarser “gray” crystalline hematite ($>5\text{--}10\ \mu\text{m}$ crystals) (Lane et al., 2002). This hypothesis is supported by the detection of hematite by CheMin in both red and gray outcrops (Rampe et al., 2020). Lastly, CheMin observes a second, notable difference between the gray and red outcrops of the Jura member with the detection of jarosite and akaganeite within the only sampled red Jura outcrop (Rock Hall drill target), but not in a nearby gray outcrop (Highfield drill target) (Rampe et al., 2020). As such, these two diverging mineralogical observations between the gray and red outcrops will need to be carefully considered in any discussion regarding the diagenetic history of the Jura member.

In summary, stratigraphic, mineralogical, and chemical observations of the VRR outcrops suggest that various processes were involved at VRR, including diagenetic processes, which are notably expressed as red to gray lateral color variations in outcrops. The results reported hereafter on small-scale diagenetic features, observed in both red and gray outcrops, provide further insights into the processes at play during the diagenesis.

3.3. Diagenesis in the Context of Gale Crater

The Curiosity rover has identified a range of mineral assemblages associated with diagenetic features, which are instrumental to reconstruct the postdepositional history of sedimentary deposits at Gale crater. Most notable among these features are the millimeter- to cm-wide light-toned Ca-sulfate veins observed throughout the traverse, across all stratigraphic members, which represent a late stage of diagenetic activity (L'Haridon et al., 2018; e.g., Nachon et al., 2014). In the Bradbury formation, at Yellowknife Bay (Figure 1), the light-toned veins are composed of nearly pure Ca-sulfate and have therefore been interpreted as precipitation from a fluid that dissolved preexisting, more impure Ca-sulfate deposits (Schwenzer et al., 2016). Within the mudstones of the Murray formation (Figure 1), the light-toned veins are more pervasive and were interpreted to have formed by hydraulic fracturing (Caswell & Milliken, 2017; De Toffoli et al., 2020). There, the light-toned Ca-sulfate veins are locally associated with Mg-sulfates, Fe-sulfates, fluorite (Nachon et al., 2017), as well as P- and Mn-rich mineral phases (Meslin et al., 2018). In addition, large silica-rich haloes are observed along fractures crossing through the Murray formation and the overlying eolian sandstone of the Stimson formation (Figure 1) (Frydenvang et al., 2017).

The variability in compositions and textures of the diagenetic features and their distribution across the Murray formation attest to a complex history during diagenesis, with local occurrences (e.g., fluorite detections) associated with more pervasive features (Ca-sulfate veins). There, diagenesis involved multiple stages of groundwater circulation with varying fluid compositions that are still only partly understood. In this context, the formation of hematite in association with light-toned Ca-sulfate veins locally at VRR constitutes an important piece of the puzzle and raises questions with respect to the diagenetic history of VRR compared to the rest of the Murray formation.

4. Results

In order to contextualize ChemCam chemical and spectral observations, each type of small-scale diagenetic feature encountered on the ridge will first be described thoroughly with the help of both RMI and MAHLI images (section 4.1). However, as the textures and morphologies of the diagenetic features directly relate to their chemical (and mineralogical) compositions, the descriptions will also introduce key observations on chemical composition, which will be further detailed in the subsequent sections (sections 4.2 and 4.3).

4.1. Description and Major Element Chemistry of Diagenetic Features

4.1.1. Light-Toned Veins

Pervasive to all geological terrains explored so far by the *Curiosity* rover, millimeter- to centimeter-scale light-toned mineralized veins are consistently observed across VRR. The Pettegrove Point member is dominated by curvi-planar light-toned veins and erosion resistant fins, which transition upward to more recessive fine veins and fracture fills in the Jura member (Bennett et al., 2020), all clearly diagenetic since they disrupt

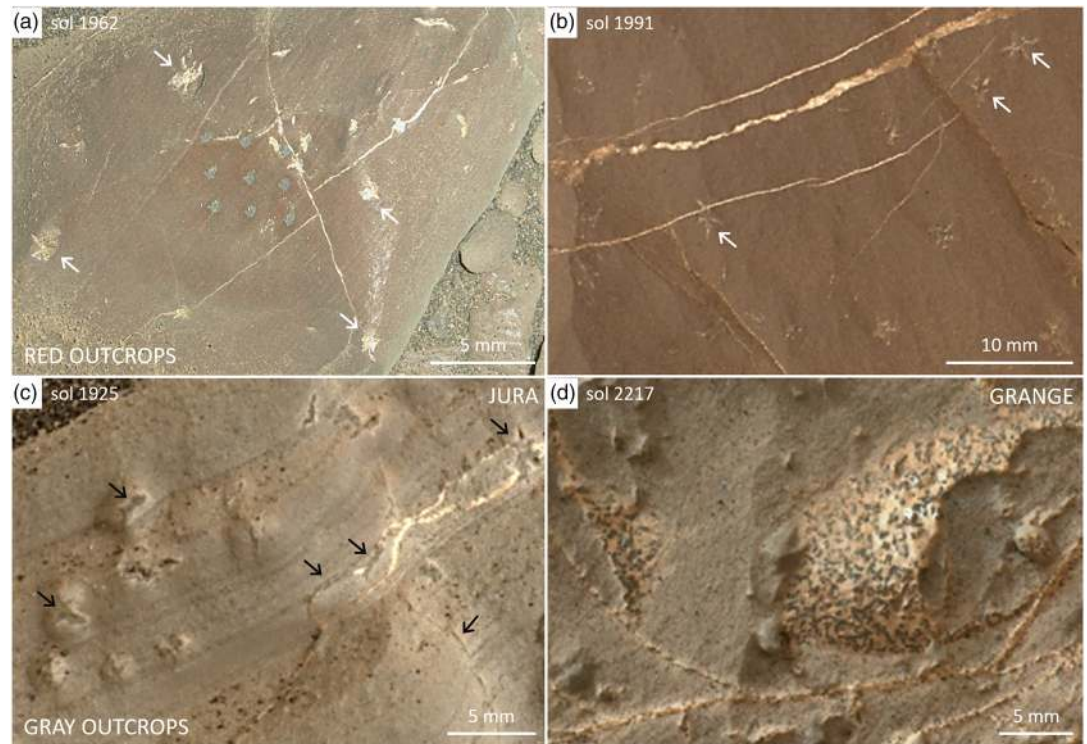


Figure 2. MAHLI observations of light-toned veins in the Jura member of VRR. In red outcrops: light-toned veins crosscutting light-toned crystals (white arrows) with shapes consistent with gypsum habit (a, b), which in some locations also incorporate hints of darker-toned material (b). In gray outcrops: dark-toned material observed as partial fills in light-toned veins and in angular crystal casts (black arrows) (c), as well as polygonal inclusions within “wandering” light-toned veins (d). MAHLI images: 1962MH0001630000704514R00 (a), 1991MH0001900010800121C00 (b), 1926MH0003690000703349R00 (c), and 2217MH0007060010802994C00 (d).

primary sedimentary structures (i.e., subhorizontal bedding, lamination, and cross-bedding). In addition, the morphology of the fracture network exhibits no clear preference for orthogonal intersections, with light-toned fractures that often “wander” and isolate host rock fragments. Similar morphologies were also observed in the terrains below the ridge, where light-toned veins are interpreted to have formed by hydraulic fracturing, induced by pore-fluid pressure build-up in a compacting sedimentary basin (Caswell & Milliken, 2017; De Toffoli et al., 2020; Kronyak et al., 2019). The composition of the light-toned veins is strongly enriched in sulfur and calcium, thus consistent with Ca-sulfate mineralogy (cf. section 3.2), in line with the previous observations on similar features along the rover traverse (Nachon et al., 2014; Rapin et al., 2016).

Lateral variations of vein texture and composition are notably observed in the Jura member. In the red outcrops, the thin straight fracture-filling veins are recessive with a smooth texture and uniformly white color (Figures 2a and 2b). In contrast, in the gray outcrops, the veins *Curiosity* encountered display a rugged texture, often encompassing dark-toned polygonal inclusions and partial vein fills (cf. section 4.1.3 and Figures 2c and 2d).

Lastly, *Curiosity* observed large light-toned veins within the gray outcrops that encompass gray-toned diffuse patches where ChemCam measured high FeO_T content in addition to their Ca-sulfate component (Figure 3). These observations are reminiscent of Fe enrichments observed within light-toned Ca-sulfate veins lower in the Murray formation (L’Haridon et al., 2018).

4.1.2. Angular Crystal Casts

Both red and gray outcrops host angular, millimeter-scale crystal casts (e.g., Figures 2a–2c and 4) (Bennett et al., 2020). While individual casts are observed as euhedral tabular crystal shapes, they commonly coalesce into V-shaped (or “swallowtail”) and star-shaped crystalline aggregates (Figures 2a–2c and 4). Though

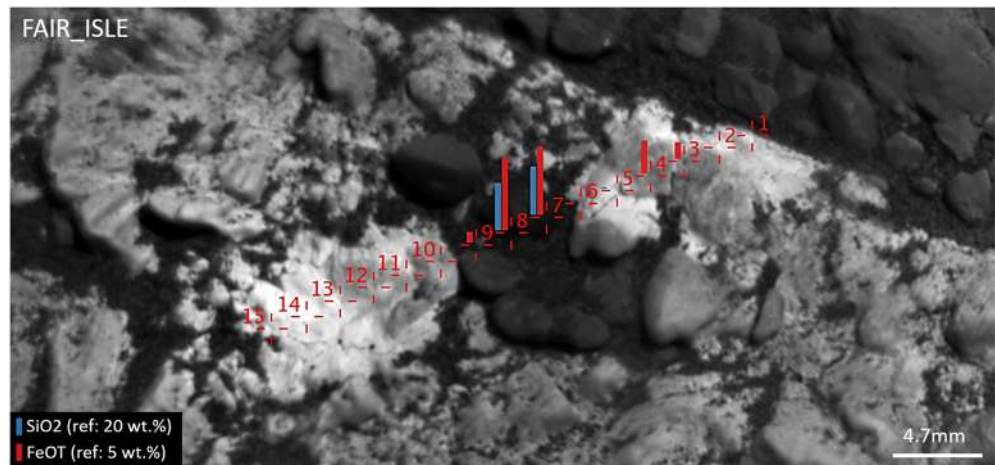


Figure 3. ChemCam analyses on a large light-toned Ca-sulfate vein (Fair_Isle target) show diffuse Fe enrichment associated with grayer material within the vein (around Points 3 and 4), in the gray outcrops of the Jura locality. FeO_T and SiO_2 relative contents for each ChemCam sample location are indicated (the red and blue bars in the legend indicate the reference, set at 20 wt.% for SiO_2 and 5 wt.% for FeO_T) to illustrate that the enrichment in FeO_T observed in the vein (Points 3 and 4) is not correlated to an enrichment in SiO_2 . In contrast, the large variations in composition on Locations 7 and 8 reflect the sampling of wind-blown sand (the enrichment in FeO_T is correlated to an enrichment in SiO_2), so these two points will not be considered in the discussion.

crystal twinings were not identified with absolute certainty in the VRR outcrops, the observed geometry could be consistent with the crystal habit of gypsum (El-Tabakh et al., 1997; Paik et al., 2007; Warren, 2016). In the red outcrops, crystal casts exhibit a light-toned color, strikingly similar to the adjacent light-toned veins (Figures 2a and 2b), suggesting a similar Ca-sulfate composition that would be consistent with the inferred gypsum crystal habit. Unfortunately, the light-toned crystal casts observed in the red outcrops were not successfully sampled by the ChemCam instrument due to ChemCam targeting uncertainties and their small size. The light-toned crystals observed in some red outcrops also exhibited hints of replacement by a

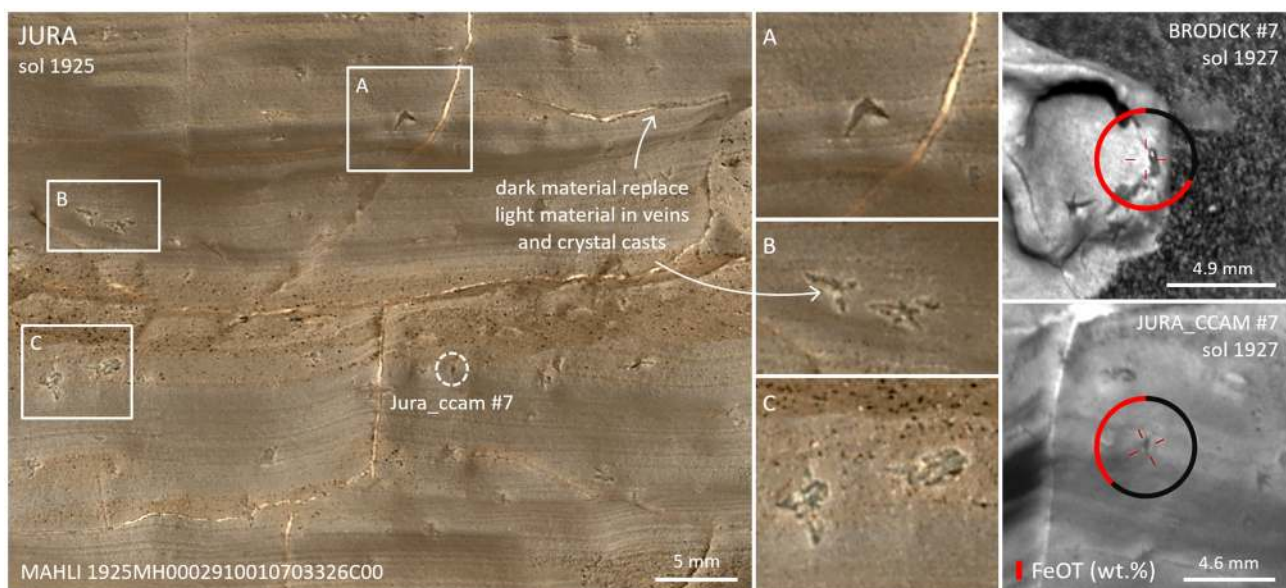


Figure 4. Crystal shapes and molds observed on sol 1927 (“Jura” locality, within gray outcrops) showing swallowtail-like shapes (inset a) as well as star-shaped aggregates (insets b and c) reminiscent of gypsum crystal habit. These features were sampled by ChemCam on the Brodick 7 and Jura_ccam 7 targets and show enrichment in FeO_T (59.6 and 34.5 wt.%, respectively, corresponding to the red section of the circles around the target) compared to the host rock (~20 wt.%).

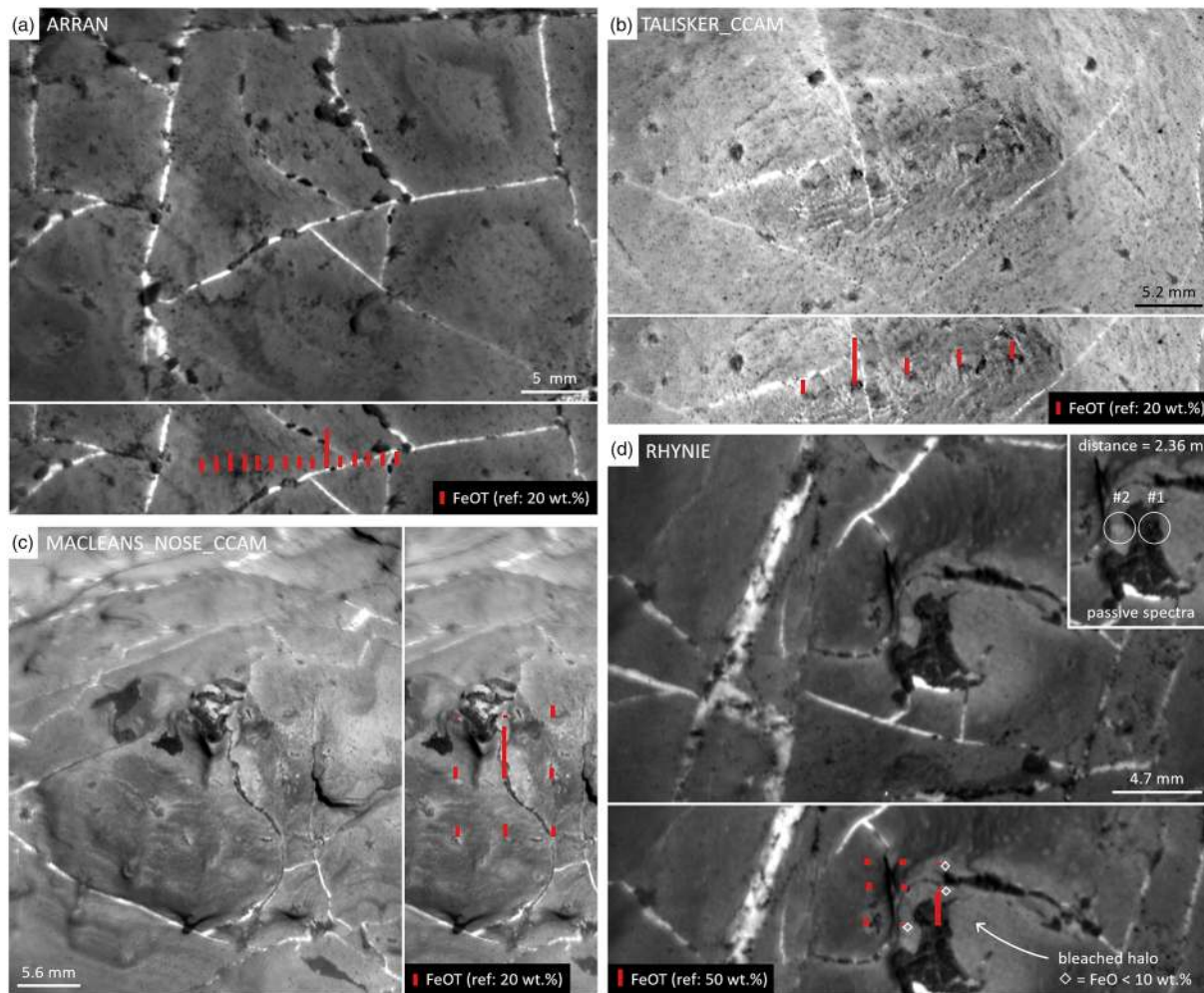


Figure 5. ChemCam observations of dark-toned features, encountered preferentially along light-toned Ca-sulfate veins (e.g., a and b). Nodular dark-toned features are also observed (e.g., c and d) forming connected diagenetic complexes with dark- and light-toned veins. Dark-toned features are encountered as inclusions or partial fills in light-toned veins but are not intersected or crosscut by these veins. Dark-toned angular casts are also observed in the host rock. The host rock near the larger dark-toned features appears lighter toned (bleached halos, e.g., d). FeO_T relative contents for each ChemCam sample location illustrate the association of high Fe compositions with dark-toned features and low Fe compositions with bleached light-toned halos (the red bar in the legend indicates the reference, set at 20 wt.% for a, b, and c and 50 wt.% for d). The field of view for passive observations is indicated on the Rhyynie target, for the observation points 1 (dark-toned Fe-rich feature) and 2 (low-Fe bleached light-toned halo).

darker-toned material (Figure 2b). In contrast, the crystal-shaped casts encountered in the gray outcrops are mostly expressed as void spaces (crystal molds) or comprise mainly dark-toned material with hints of residual light-toned material (Figures 2c and 4; the residual light-toned material is notably visible in inset b). ChemCam was more successful in targeting these dark-toned angular crystal casts, reporting a composition enriched in FeO_T (Figure 4).

The euhedral crystal casts appear to be randomly distributed in the host rocks, with no preferred orientation with respect to bedding planes (e.g., Figure 4). Additionally, at the MAHLI image resolution, the casts do not appear to disrupt primary sedimentary structures (e.g., laminations on Figures 2a–2c and 4), which would have indicated displacive mineral growth within unconsolidated sediments (Hardie, 1985; Murray, 1964; Warren, 2016).

4.1.3. Dark-Toned Polygonal Features and Fracture Fills

The gray outcrops also host dark-toned nodular features (Figure 5) that are characterized by high FeO_T abundances (cf. section 4.2). These features are preferentially encountered along light-toned veins, as inclusions and fracture fills (Figures 2c, 2d, and 5) but are also observed scattered in the adjacent host rock (e.g.,

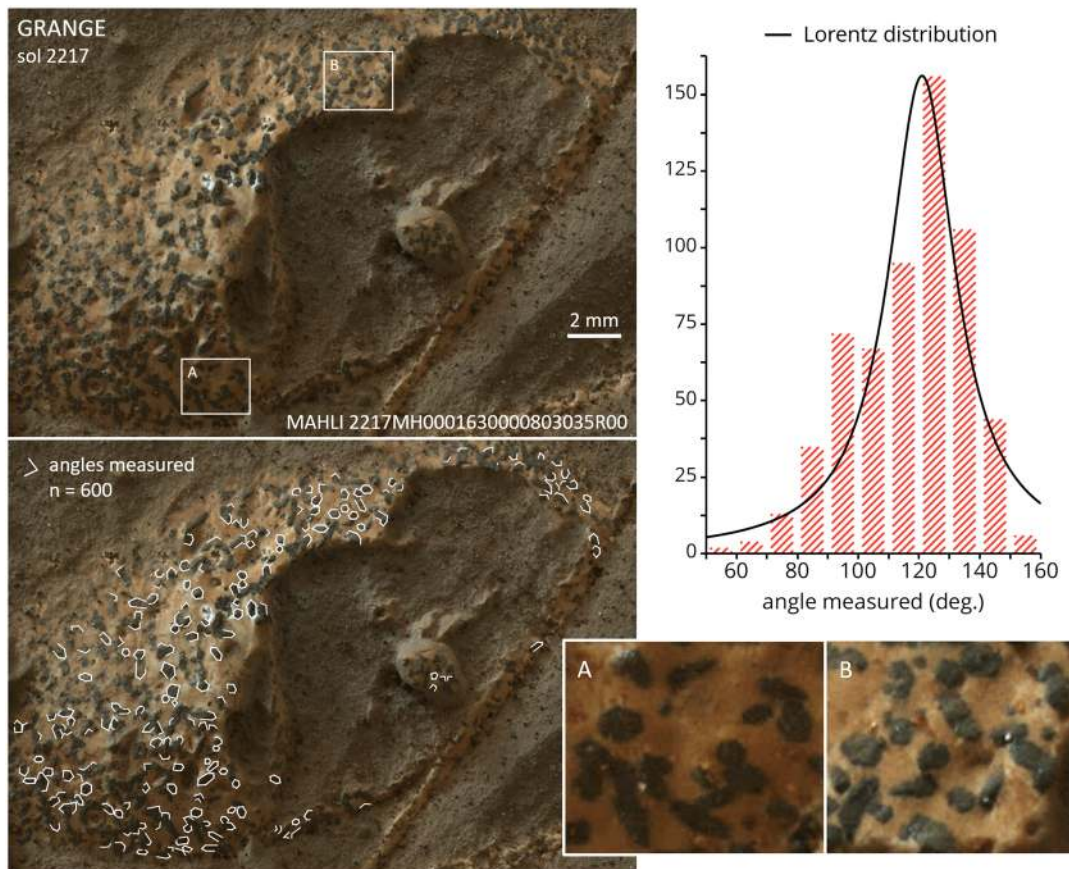


Figure 6. Morphological analysis of dark-toned crystals in the Grange target (left). The angles measured on identifiable crystals (white lines, bottom left) show a distribution centered around 120° (right). This distribution of angles would be consistent with a hexagonal crystal family and reflects the numerous hexagonal shapes observed on the dark-toned crystals (i.e., insets a and b).

Figures 4 and 5a–5c) displaying angular shapes similar to the light-toned crystals observed in the red outcrops (cf. section 4.1.2). Interestingly, the host rock in close proximity to some of the largest dark-toned features is lighter toned (or bleached) over a few millimeters (e.g., around the larger nodular dark-toned features and adjacent fracture fills; Figures 5c and 5d) with lower FeO_T content compared to the surrounding bedrock.

Fracture fills transition laterally from light-toned to dark-toned material within the same fracture (e.g., Figures 2c, 5c, and 5d) and light-toned veins never crosscut the dark-toned features (Figures 2c and 5). Furthermore, the dark-toned inclusions observed within the “Grange” target, a light-toned vein (Figures 2d and 6), present euhedral crystal shapes. The dark-toned inclusions display a hexagonal crystal habit, as denoted by the elongated hexagonal prism and regular hexagon shapes associated with the dark-toned euhedral crystals within the light-toned “Grange” vein (Figures 6a and 6b). In addition, the angles measured on unambiguous dark-toned crystals within the vein ($n = 600$) show a distribution with a median at $\sim 120^\circ$ (Figures 6), and an elevated number of angles near 90° . Such a distribution of angles suggests that the dark-toned mineral pertains to the hexagonal crystal family (three axes of symmetry with an included angle of 120° and a fourth axis perpendicular to the others).

Lastly, *Curiosity* observed dark-toned polygonal and elongated features that protrude from the gray outcrops in positive relief, along fracture planes, reflecting a higher resistance to erosion than the surrounding host rock. ChemCam sampled only once these erosion-resistant features—which displayed elevated FeO_T (Haroldswick 17 inset, Figure 7)—although the feature appears to have been eroded by the successive laser shots. The morphological similarities with neighboring dark-toned features (notably polygonal fracture fills)

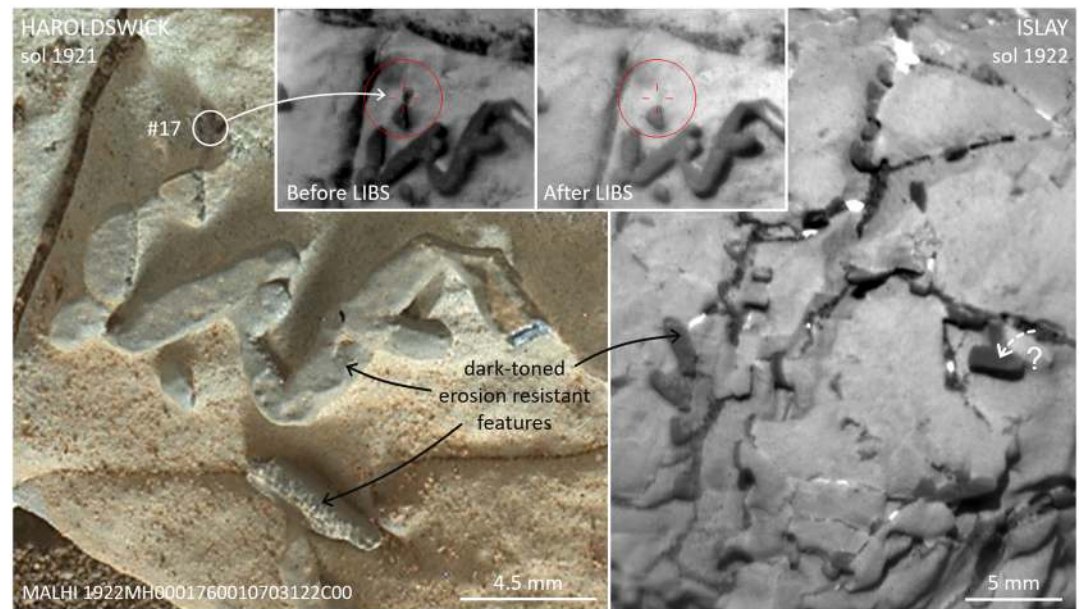


Figure 7. Polygonal and elongated erosion-resistant dark-toned features (“stick-shaped”) observed at the “Jura” locality within gray outcrops, which show morphological similarities with high-Fe dark-toned features (notably fracture fills) and potentially associated with polygonal molds observed along fractures (e.g., Islay target). ChemCam may have sampled a dark-toned erosion-resistant feature (inset; Haroldswick 17), which showed elevated Fe abundances (~39 wt %) but was eroded by the ChemCam laser shots.

and with adjacent polygonal molds observed along fractures (e.g., Islay target, Figure 7) suggest a genetic link between these features (Bennett et al., 2020).

4.2. Detailed Chemistry (Major and Minor Elements) of Diagenetic Features

The chemical abundances from ChemCam are reported in ternary diagrams in Figure 8 (in molar proportion, based on quantified oxide weight percent reported by ChemCam), illustrating the chemical trends between Fe and Si with respect to Al, Mg, and Ca (Figures 8a, 8c, and 8d) and between Fe, Si + Al, and Mg + Na + K (Figure 8b). This data set includes observations on host rock (3,175 points), light-toned veins (207), dark-toned features (101), and bleached host rock (71) (see section 2.2).

The dark-toned features, including dark-toned material within angular crystal casts, show a composition dominated by enrichment in Fe and corresponding decreases in other major elements (notably Si, Al, Mg, K, and Na) compared to the host rock compositions (Figures 5 and 8). High-Fe observations are not associated with the detection of elements that may form volatile compounds (S, Cl, P, F, or C; Figure S1 in the supporting information), ruling out any Fe sulfates or Fe phosphates (Forni et al., 2015; Meslin et al., 2018; Nachon et al., 2016). The H emission line is also relatively low (Figure 9), thus pointing toward poorly hydrated Fe-oxide minerals.

The only exception was observed on St Cyrus 8, (Figure S1) where high Fe is associated with Cl and high H, and which is interpreted as a detection of akaganeite [FeO (OH,Cl)]. That observation was however not clearly associated with an identifiable dark-toned feature (Figure S1) and thus interpreted to reflect the presence of akaganeite in the host rock, which was also observed by the CheMin instrument at the Rock Hall drill site (Rampe et al., 2020).

The trend in major elements shows enhanced Fe abundances in dark-toned features, scattered along a mixing line between the host rock compositions and the Fe apex of the diagram, due to the small size of these features (laser shots on the diagenetic features also include some of the surrounding host rock). The composition of these diagenetic features trends toward a pure Fe-oxide end-member composition (Figure 8).

The spread observed toward elevated Ca in some of these features (Figure 8a) is attributed to the sampling of both dark-toned features and light-toned veins by the same ChemCam observation point, due to their close

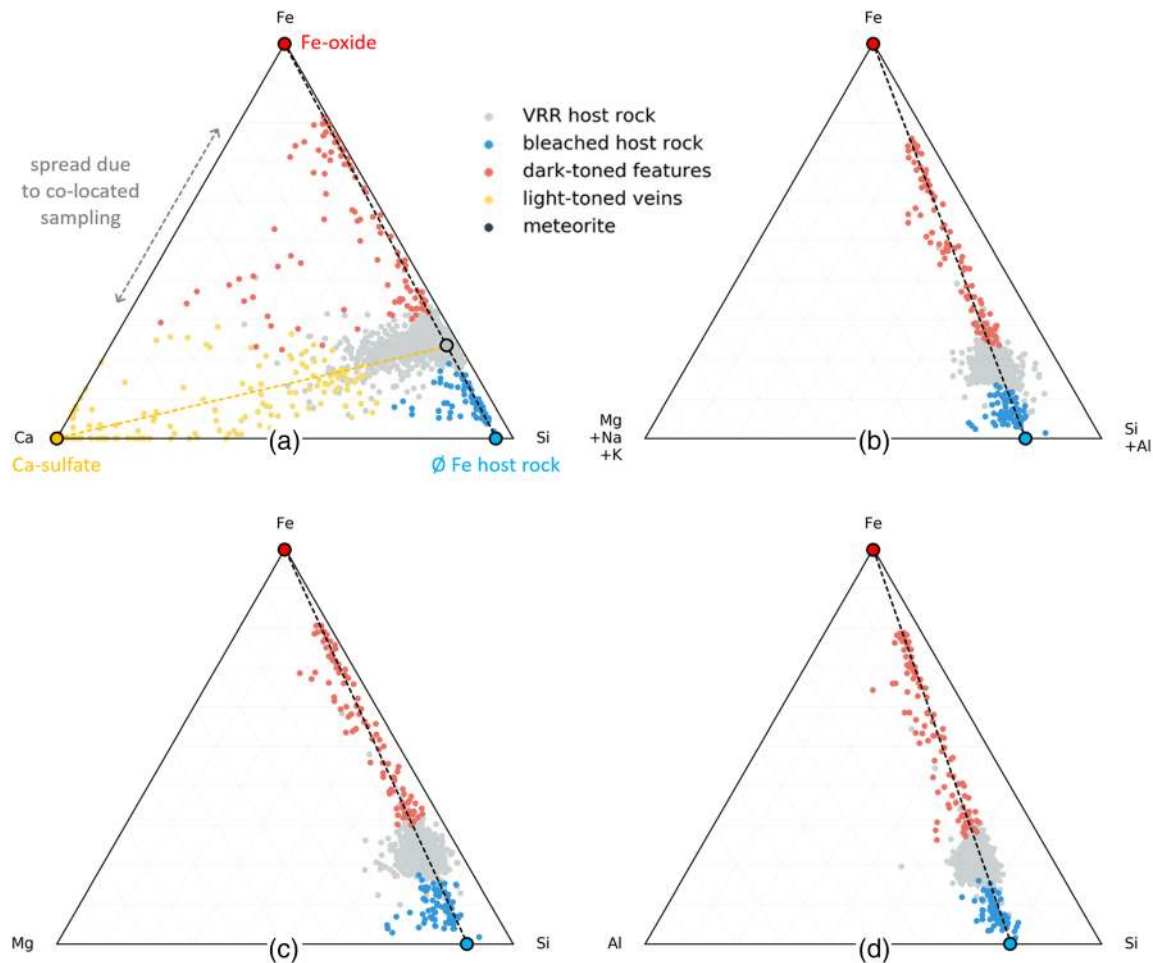


Figure 8. Ternary diagrams showing ChemCam quantified abundances (molar percentages) for major elements: dark-toned features (in red) are associated with very high Fe content, trending toward a pure Fe composition, coupled with low-Fe observations on bleached light-toned halos. Diagram (a) shows a spread toward Ca for dark-toned features due to the contribution of Ca-sulfate from adjacent light-toned veins, and sampling at the interface between both features. Diagrams (b), (c), and (d) show that the low-Fe content in the bleached host rock targets is not associated with a loss in any other major elements, suggesting that Fe was mobilized from the host rock.

spatial association (Figures 4 and 5). Indeed, light-toned veins show a composition consistent with a Ca-sulfate dominated composition (Figure 8a), with high Ca content associated with a lower sum of oxides and S detection (Nachon et al., 2014), interpreted as bassanite ($\text{CaSO}_4 \cdot 0.5 \text{H}_2\text{O}$) based on the H content detected by ChemCam (Rapin et al., 2016). In addition, some large veins also encompass gray patches that display high Fe abundances in association with Ca sulfate (cf. section 4.1.1 and Figure 3).

The lighter-toned bleached halos observed in the host rock surrounding several high-Fe dark-toned features (e.g., Rhynie 2, Figure 5) show depleted Fe content compared to other VRR host rock observations (commonly <10 wt.% compared to the 18–20 wt.% typically observed in the host rocks, Figures 5c, 5d, and 8). Interestingly, lower FeO_T abundances are not correlated with a depletion in any other major elements, which preserve the same relative abundances (Figure 8). As such, these observations suggest the preferential leaching of Fe in these bleached halos compared to the adjacent host rock composition.

Minor element abundances reported by ChemCam show mostly depleted contents in dark-toned Fe-rich features for Ba, Rb, Sr, and Li compared to VRR host rock values, whereas low-Fe bleached halo abundances for the same elements are within range of host rock values, except for a slight enrichment in Ba and Sr (Figure 9). In contrast, MnO abundances in dark-toned features are within the range of host rock values but depleted in low-Fe bleached halos (Figure 9), showing that the two redox-sensitive elements Fe and Mn are depleted in concert, while other elements are in stable abundance.

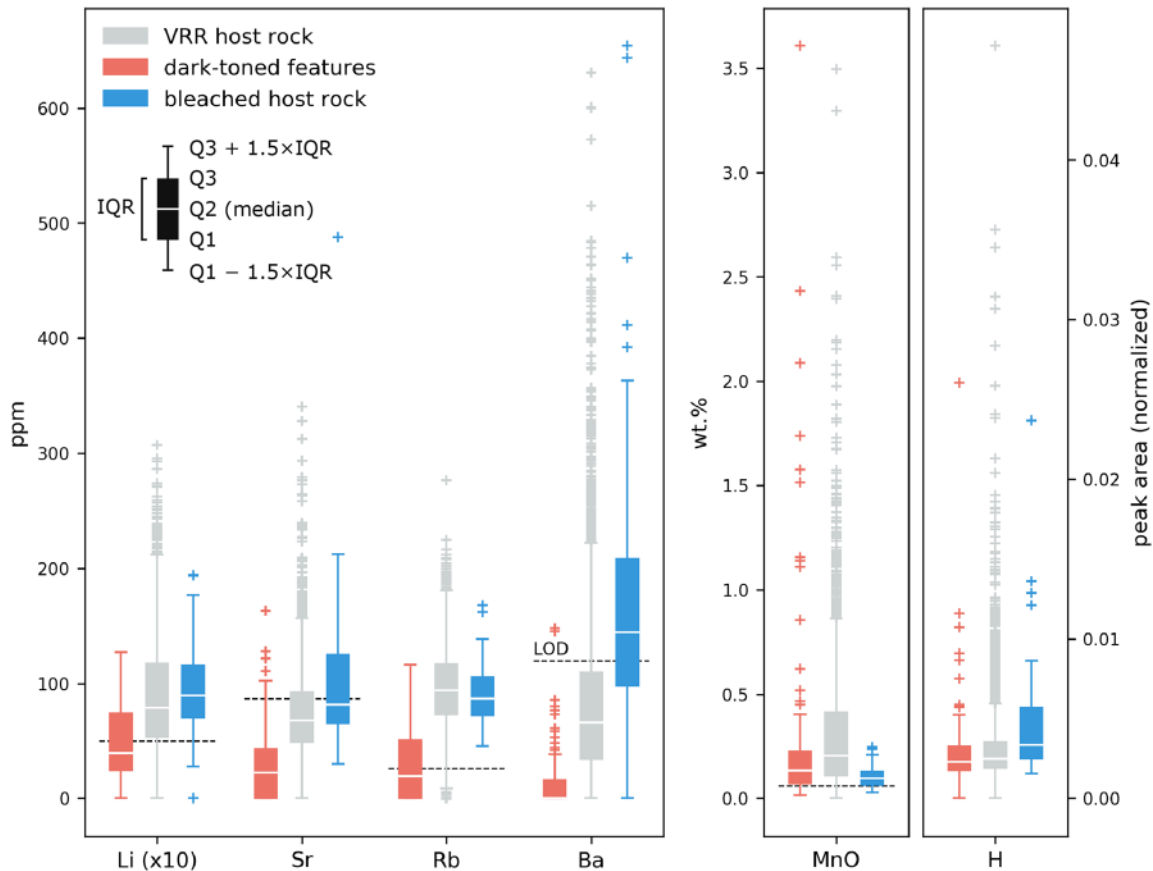


Figure 9. Box plots representing quantified abundances for Li, Rb, Sr, Ba, and MnO, as well as H normalized peak area (cf. Rapin et al., 2017), in dark-toned Fe-rich features (red), VRR host rocks (gray), and low-Fe bleached host rocks (blue). Abundances in Ba, Rb, Sr, and Li for bleached low-Fe targets are in range with typical host rock values (although slightly enriched in Ba and Sr) but are depleted in dark-toned Fe-rich features. However, MnO abundances in dark-toned Fe-rich features are in line with host rock values and appears depleted in low-Fe bleached targets. H content appears to be in line with the low host rock values in dark-toned Fe-rich features but slightly enriched in low-Fe bleached targets. Limits of detection (LODs) are indicated for Li, Sr, Rb, and Ba (Payré et al., 2017), as well as for MnO (Lanza et al., 2014).

4.3. Passive Spectra Observations

ChemCam passive spectral analyses on the various rocks of the ridge reveal variability in the strength of the spectral features diagnostic of ferric iron (i.e., absorption bands near 535 and 670 nm and a downturn after ~750 nm). Red and purple VRR host rocks show a ferric signature in passive reflectance spectra, including the red outcrops of the Jura member (Figure 10), consistent with the presence of ferric phases, and in particular hematite (Fraeman et al., 2013; Jacob et al., 2020; Johnson et al., 2017).

In contrast, the passive spectra observed in the gray outcrops are much flatter in the 600–800 nm spectral region (Figure 10). This observation is also consistent with Mastcam multispectral observations of gray outcrops and a few resolved dark diagenetic features, which also show relatively flat spectra without clear absorption bands, even at longer wavelengths not detectable by ChemCam (Horgan et al., 2020). Coarse-grained and crystalline “gray” hematite would be consistent with such passive spectral observations (cf. USGS and RELAB reference spectra, Figure 10) since grain size, crystallinity, and contaminants can also impact spectral ferric features (Johnson et al., 2015; Lane et al., 2002; Morris et al., 1985). The spectral variations observed by ChemCam and Mastcam may thus reflect the differences in mineralogy observed by CheMin (Rampe et al., 2020; Horgan et al., 2020), notably concerning the Fe-oxide components. The “red” hematite [$\alpha\text{-Fe}^{3+}_2\text{O}_3$] characterized by its ferric spectral signature in the red outcrops is giving way to “gray” crystalline hematite [$\alpha\text{-Fe}^{3+}_2\text{O}_3$] associated with a subdued spectral signature in the gray outcrops (Rampe et al., 2020). Low-Fe bleached halos do not show any spectral evidence for the presence of ferric iron, in line with the observations on the adjacent gray host rocks (Figure 10). Similarly, the relatively flat passive

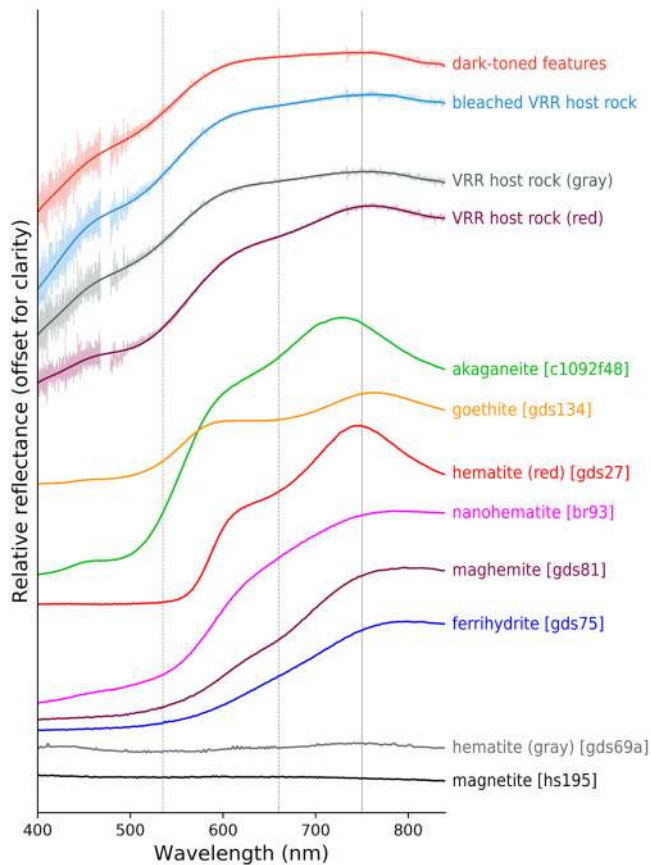


Figure 10. Passive reflectance spectra of high-Fe dark-toned features (in red, Rhynie 1) and low-Fe bleached halo (in blue, Rhynie 2), as well as gray (in gray, Ben Loyal 5) and red (in purple, Holyrood 1) host rock targets. The solid line over the spectral data corresponds to a 15th-order polynomial fit, shown here for clarity. High-Fe dark-toned features, low-Fe bleached halos, and gray host rocks lack adsorption bands near 535 and 670 nm (dashed gray lines) and a downturn after 750 nm (solid gray line) associated with Fe^{3+} phases, as observed on red host rocks. Library spectra for hematite [$\alpha\text{-Fe}_2\text{O}_3$] (red, gray, and nanophase), maghemite [$\gamma\text{-Fe}_2\text{O}_3$], magnetite [$\text{Fe}^{2+}\text{Fe}^{3+}_2\text{O}_4$], ferrihydrite [$\text{Fe}^{3+}_2\text{O}_3 \times 0.5\text{H}_2\text{O}$], goethite [$\alpha\text{-FeO}(\text{OH})$], and lepidocrocite [$\gamma\text{-FeO}(\text{OH})$] from the USGS database, as well as akaganeite [$\text{Fe}^{3+}\text{O}(\text{OH},\text{Cl})$] from the RELAB database, are provided for comparison. The laboratory spectra are scaled at half intensity, and all spectra are offset for clarity.

reflectance spectra (i.e., lacking ferric absorption features) associated with dark-toned Fe-oxide features suggest the presence of either mixed-valence Fe-oxide (i.e., magnetite) or coarse-grained gray hematite (Figure 10).

4.4. Summary of Observations

The examination of the texture and composition of small diagenetic features at VRR enables an exhaustive classification (Table 1). Overall, the light-toned veins are composed of Ca-sulfate with local and discrete enrichments in FeO_T . The abundant dark-toned features are present throughout the gray outcrops as neo-formed crystals or mineral pseudomorphs in the host rock and along the light-toned veins as partial fracture fills and nodular inclusions. These features display a unique composition consistent with anhydrous iron oxides. The passive reflectance observations lack a ferric spectral signature, which enables us to discard the presence of “red” hematite but does not help to discriminate between crystalline hematite and magnetite. Nevertheless, the hexagonal habit observed on Fe-oxide dark-toned crystals within light-toned veins (Figure 6) provides insights into the crystalline structure of the observed Fe-oxide, which would be consistent with gray hematite, but not with magnetite. Indeed, hematite crystallizes in the trigonal system (part of the hexagonal family) and is commonly observed as hexagonal platelet-type crystals (Cornell & Schwertmann, 2003; Sugimoto et al., 1996, 1993), while magnetite crystallizes in the cubic system and almost exclusively forms octahedral crystals (Cornell & Schwertmann, 2003).

Diagenetic mineral replacements (pseudomorphism) appear to be limited to the gray outcrops, as the light-toned crystal casts observed in the red outcrops only show very limited evidence for dissolution and/or mineral replacement (cf. Figure 2b). So are dark-toned fracture fills, which are scarcely observed outside of the gray outcrops. The bleached halos observed in the host rock surrounding some of the larger hematite-rich dark-toned features may give insights into the diagenetic processes that occurred in the gray outcrops. The high- FeO_T and low- FeO_T observations (respectively, dark-toned features and bleached halos) neatly plot along a mixing line between Fe-oxide and “Fe-free” host rock compositions, suggesting that Fe was mobilized locally from the host rock to form the Fe-oxide dark-toned features during diagenesis. Fe and Mn appear to exhibit a similar behavior, which would be consistent with the involvement of redox-driven chemical processes in the formation of these features since Mn mobility also greatly depends on its oxidation state (e.g., Post, 1999). Higher temperatures may also enhance the mobility of these elements,

as it was suggested from CheMin analyses (Rampe et al., 2020), but the hydration of Ca-sulfates observed in light-toned veins (mostly basanite) indicates that temperatures did not exceed 60°C at the time of their formation (Rapin et al., 2016, and references therein). This observation, together with the lack of mobility in other elements, exclude a high-temperature scenario for the later stages of diagenesis at least, which are associated with the formation of hematite dark-toned features and crystals alongside Ca-sulfate veins.

The morphological similarities between these neighboring dark-toned features suggest a genetic link between them. Observations of mineral pseudomorphs suggest that hematite replaced the original light-toned mineral (likely gypsum) during diagenesis—preserving its initial crystal shape through dissolution (formation of empty crystal molds) and recrystallization (e.g., Lougheed, 1983; Paik et al., 2007). The observations of pseudomorphism and low-Fe bleached halos around the dark-toned features suggest chemical interactions and Fe mobility within the host rock at the time of their formation. In contrast, the presence of dark-toned partial fracture fills and dark-toned inclusions in the Ca-sulfate veins indicate a relationship with the stage of fracturing and vein formation during diagenesis. Accordingly, the observations of

Table 1
Summary of Diagenetic Observations on Vera Rubin Ridge

	Feature	Description (section 4.1)	Composition (sections 4.2 and 4.3)
Red outcrops	Light-toned veins	<ul style="list-style-type: none"> • linear and thin morphology • smooth texture, uniform white color • crosscut primary sedimentary structures and angular crystal casts 	<ul style="list-style-type: none"> • high Ca and S, variable Sr • H consistent with bassanite
	Angular crystal casts	<ul style="list-style-type: none"> • euhedral and tabular crystal shapes form V-shaped and star-shaped aggregates • uniform white color (similar to light-toned veins) primary sedimentary structures not deformed • exhibits hints of replacement by darker-toned material in some outcrops 	<ul style="list-style-type: none"> • no data (inferred to be Ca-sulfate)
Gray outcrops	Light-toned veins	<ul style="list-style-type: none"> • rugged texture • encompass dark-toned inclusions, partial fills, and diffuse gray patches • crosscut primary structures, but not dark-toned features or dark-toned pseudomorphs 	<ul style="list-style-type: none"> • high Ca and S, variable Sr • H consistent with bassanite • high Fe for dark-toned inclusions, partial fills and gray patches
	Angular crystal casts	<ul style="list-style-type: none"> • euhedral and tabular crystal shapes form V-shaped and star-shaped aggregates • occasionally observed as crystal molds • substitution of precursor light-toned material by dark-toned material (pseudomorphism) • primary sedimentary structures not deformed 	<ul style="list-style-type: none"> • elevated Fe compared to host rock (dark-toned material)
	Dark-toned features, fracture-fills, and erosion-resistant casts	<ul style="list-style-type: none"> • nodular features observed in association with light-toned veins (inclusions and fracture-fills) • polygonal and elongated casts resistant to mechanical erosion, possibly match adjacent polygonal molds along fractures • dark-toned inclusions display hexagonal crystal shapes, possibly pertaining to the hexagonal family (distribution of angles around 120°) 	<ul style="list-style-type: none"> • very high Fe, low H • Mn at a similar level compared to host rock composition • depleted in other elements • lack ferric absorption bands
	Bleached halos	<ul style="list-style-type: none"> • lighter-toned halos in the host rock • observed around the larger dark-toned nodular features and fracture-fills 	<ul style="list-style-type: none"> • low Fe and low Mn • other elements in line with the host rock composition, except for slightly elevated Ba and Sr • lack ferric absorption bands

euhedral dark-toned Fe-oxides within a large Ca-sulfate vein at “Grange” indicate that the dark-toned inclusions and the light-toned veins formed contemporaneously, which constitutes a critical observation in order to determine the chronology of the diagenetic episodes (section 5.1) as well as mineral parageneses (section 5.2).

5. Discussion

5.1. Diagenetic History of VRR

The VRR sedimentary rocks, deposited in a lacustrine environment, record a complex postdepositional geological history, as evidenced by the variety of small-scale diagenetic features observed on the ridge (Table 1). Crosscutting relationships between the observed diagenetic features, and how they affect the primary sedimentary structures, provide insights into their relative timings of formation. Thus, we discuss here the formation of the geological features observed on VRR, to reconstruct the sequence of events that occurred during its diagenetic history (Figure 11).

The VRR sedimentary rocks form a topographic high because they are harder and more resistant to erosion compared to the surrounding terrains. A possible explanation for such properties would be the presence of a fine-grained pore-filling cement, which formed early during the diagenesis of the VRR sedimentary rocks and resulted in their lithification and hardening. Moreover, the preservation of gypsum crystals in the red

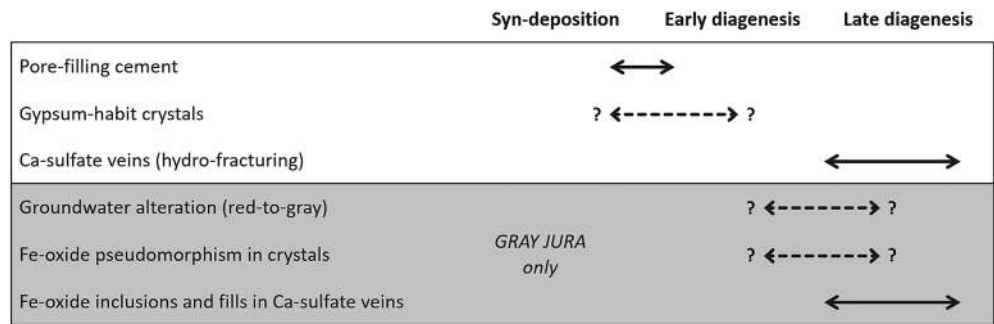


Figure 11. Paragenetic sequence of the events that occurred during the diagenesis of Vera Rubin ridge.

outcrops of the Jura member suggests that cementation was either contemporaneous with the formation of such crystals or involved limited fluid circulations in order to prevent the dissolution of the preexisting evaporite minerals (Murray, 1964; Warren, 2016). As such, cementation likely occurred in the interstitial waters of the sediments in the early stages of diagenesis.

The lateral variations observed in the VRR outcrops (Figure 1), in the form of red to purple to gray color gradients, are attributed to a change in the mineralogy or crystallinity of these rocks (Horgan et al., 2020). These lateral variations do not appear to be related to changes in the depositional lacustrine environment (Edgar et al., 2020) and are thus inferred to be diagenetic in origin, involving groundwater flow. As the ability of fluids to propagate through the sedimentary rocks depends on their permeability, the formation of the red-to-gray alteration patterns probably occurred before significant compaction and lithification of the sediments reduced drastically the connected porosity (i.e., before late diagenesis). Lastly, the coarser grain sizes observed on the gray outcrops, compared to the adjacent finer-grained red outcrops (Bennett et al., 2020; Edgar et al., 2020), would have also favored the propagation of fluids during diagenesis.

The timing of the formation of Ca-sulfate minerals may be difficult to assess, as it can crystallize either by evapo-concentration near the surface or by reactions of dissolution and reprecipitation at depth due to its solubility, creating a variety of textures (Hardie, 1985). The gypsum-habit crystals observed within the VRR outcrops, displaying euhedral crystals morphologies (cf. section 4.1.2), could either reflect unimpeded crystals growth before significant compaction and lithification of the host sediments, or instead formation of poikilotopic crystals (i.e., that incorporate sediment grains) through connected porosity in more consolidated sediments later on during the diagenesis (Bain, 1990; Murray, 1964; Warren, 2016). Prior observations of Ca-sulfate enrichments in the Murray formation, below VRR in the stratigraphy, are interpreted to have formed near surface during early diagenesis due to the enrichment volume and lithology (Kah et al., 2018; Rapin et al., 2019). At VRR, the observed light-toned crystals represent a minor volume of the host rock and occur in a different lithology. Nevertheless, their formation must predate their substitution via pseudomorphism by dark-toned Fe-oxide within the gray outcrops (cf. section 4.1.2). As such, the light-toned crystals were most likely already emplaced before the formation of the red-to-gray color patterns within the VRR outcrops.

The light-toned Ca-sulfate veins are also observed throughout the VRR outcrops and are interpreted as late-diagenetic products formed by hydraulic fracturing (cf. section 4.1.1), in line with previous observations along the rover traverse. However, the diversity of textures and morphologies observed in these features (Bennett et al., 2020) could indicate multiple successive episodes of fracturing and mineralization (Caswell & Milliken, 2017; De Toffoli et al., 2020), or distinct interactions with the enclosing host rocks.

Lastly, the dark-toned Fe-rich features encountered within the gray outcrops are often associated with light-toned Ca-sulfate veins, as either hexagonal inclusions (Figures 2 and 6) or fracture fills (Figures 2–5), and appear to be contemporary with the formation of fractures and Ca-sulfate mineralization (cf. section 4.1.3). Low-Fe bleached halos are also observed in association with the larger dark-toned Fe-rich features in the surrounding host rock (Figure 5), which suggests the mobilization of Fe at the time of the formation of dark-toned features. In addition, the Fe-rich dark-toned features that are not associated with light-toned veins display—for the most part—angular crystal shapes that are reminiscent of the gypsum-habit crystals observed in the red outcrops and are thus interpreted as pseudomorphs. The dark-toned pseudomorphs

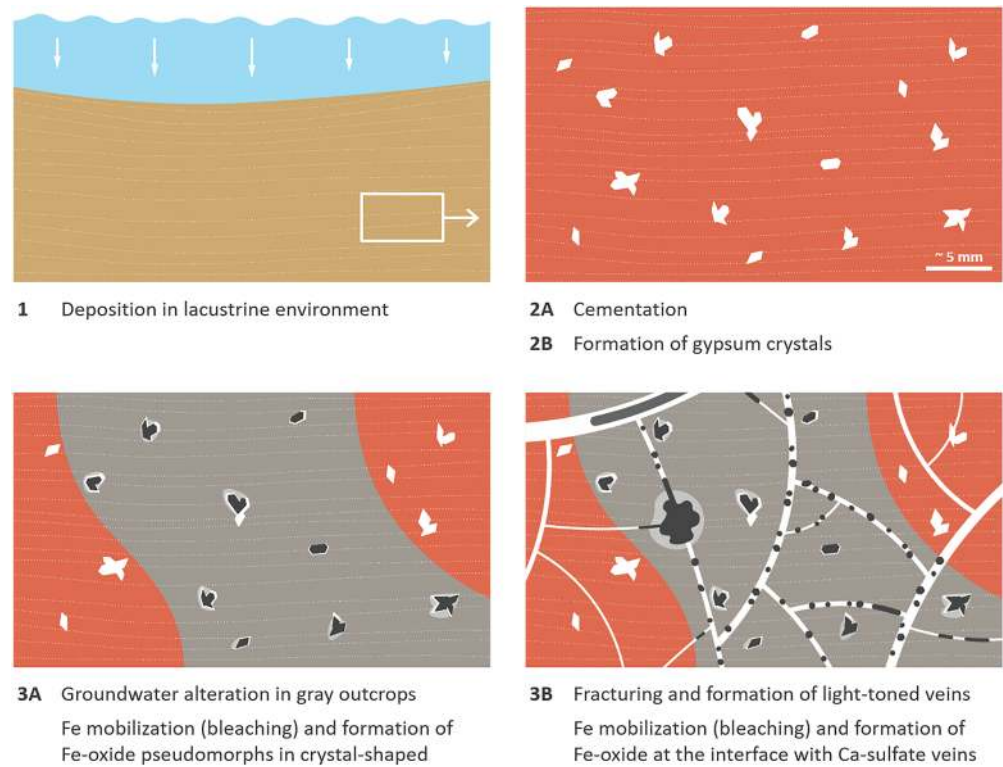


Figure 12. Schematic sequence of events involved in the formation of Vera Rubin ridge. Gray areas are represented schematically at the small scale for simplicity but can extend to several tens of meters. Panels 3A and 3B are related to the mobilization of iron to form, respectively, dark-toned pseudomorphs and dark-toned inclusions in light-toned veins (euhedral crystals and partial fills), which may correspond to either a singular event or two distinct episodes, without any definitive evidence for the former or the latter.

are not crosscut by light-toned veins (e.g., Figures 2c and 4), which indicates that pseudomorphism likely occurred during or after the emplacement of light-toned veins. Since the substitution of light-toned crystals appears to be related to the formation of gray outcrops, the relative timing between fracture formation and groundwater alteration in the gray outcrops remains ambiguous, as the two events could be coeval.

In summary, the formation of the VRR sedimentary deposits probably involved the following sequence of events (summarized in Figure 12):

1. deposition in a lacustrine setting;
2. cementation (cf. section 5.2), either during sedimentation or within the interstitial pore waters in the early stages of diagenesis (Figure 12, 2A), which occurred either before or at the same time as the emplacement of gypsum euhedral crystals (Figure 12, 2B);
3. formation of the red-to-gray color gradients within the outcrops of the ridge through groundwater alteration, which also led to the substitution of gypsum crystals by Fe-oxide pseudomorphs in the gray outcrops (Figure 12, 3A), and likely contemporaneous with the formation of Ca-sulfate light-toned veins, associated in the gray outcrops with the mobilization of Fe from the adjacent host rock and the formation of Fe-oxide as hexagonal crystals and partial fills within the light-toned veins (Figure 12, 3B).

5.2. Potential Chemical Processes During Diagenesis

The formation of small-scale dark-toned Fe-oxide features on VRR is concentrated in the Jura member, suggesting that it experienced local diagenetic processes. In this section, we explore hypotheses that could explain the formation of hematite through (i) mobilization of Fe from the adjacent host rock leading to the formation of Fe-poor bleached halos and (ii) formation of Fe-oxide in association with Ca-sulfate diagenetic features, either as inclusions in light-toned veins or as mineral substitutes to preexisting gypsum-habit

crystals. While light-toned Ca-sulfate features are encountered in both red and gray outcrops throughout VRR, their association with dark-toned Fe-oxide features is almost exclusively restricted to the gray outcrops (cf. section 4.1). As such, Fe mobilized from the adjacent gray host rock likely precipitated in the form of Fe-oxide upon interaction with Ca-SO₄ bearing fluids.

The most notable difference between red and gray outcrops—aside from their spectral properties and diagenetic components—lies in their respective Fe-bearing secondary mineralogy. Indeed, akaganeite and jarosite are identified in association with red hematite in the red outcrops but not in the gray outcrops, which instead comprise gray crystalline hematite (Rampe et al., 2020). While the mobility of Fe observed in the gray outcrops could potentially result from the dissolution of metastable ferric mineral phases (i.e., jarosite and akaganeite) by groundwater fluids, their presence throughout the Jura member is contested as the drill location displayed peculiar chemical composition and spectral properties compared to other red outcrops (David et al., 2020; Frydenvang et al., 2020; Horgan et al., 2020). In addition, the dissolution of akaganeite and jarosite alone—in the low abundances observed—could not account for the low-Fe abundances observed in the bleached halos (<10% wt.%). So we infer that other Fe-bearing minerals—notably hematite, as it is the most abundant Fe-bearing mineral phase detected by CheMin in the VRR outcrops (Rampe et al., 2020)—had to be at least partially dissolved from the host rock to account for the observed mobility of Fe in the gray outcrops.

Generally speaking, hematite can be readily dissolved by acidic (low pH) or reducing (low Eh) conditions (Cornell & Schwertmann, 2003). In this regard, the detection of reduced sulfur in the drill samples from the Jura member by the SAM instrument would support the presence of reducing conditions in the diagenetic fluids (Wong et al., 2020, and references therein). The fact that both Fe and Mn have been mobilized in the gray outcrops, whereas nonredox sensitive elements (such as Si, Al, and Mg) have not, also suggests the involvement of reducing fluids rather than strongly acidic ones. The observed variability in Fe and Mn across the VRR bedrocks (David et al., 2020; Frydenvang et al., 2020) has also been attributed to remobilization by reducing diagenetic fluids.

Reducing conditions are expected to have dominated the Noachian era of Mars, and to this day, the Martian atmosphere does not contain high abundances of oxygen (e.g., Dehouck et al., 2016, and references therein). Petrologic studies show that magmatic rocks on Mars are derived from a reducing mantle source, leading to the formation of reduced basalts (Herd et al., 2002). During sedimentation in Gale crater, stratification in the lake waters could have also enabled reducing conditions to prevail, at least locally (e.g., Hurowitz et al., 2017). In summary, it is fair to assume that reducing fluids could have carried Fe²⁺ in solution during sedimentation (Figure 12, Panel 1) and throughout the diagenesis (Figure 12, Panels 2, 3A, and 3B) at VRR. Moreover, experimental results and thermodynamic models (Baron et al., 2019) suggest that Fe²⁺ would readily oxidize to form hematite bearing, clay-dominated assemblages upon diagenetic alteration of the VRR host rocks (Figure 12, Panel 2).

The partial dissolution of preexisting hematite by reducing fluids during diagenesis would result in the release of Fe²⁺ ions in the aqueous solution. In the absence of Ca-sulfate in close proximity, Fe²⁺ mobilized from the host rock likely recrystallized in place as gray hematite, through the coarsening of existing hematite grains by Ostwald ripening (David et al., 2020; Horgan et al., 2020) (Figure 12, Panel 3A). This would explain the subdued ferric spectral properties and the mineralogy of the gray outcrops (Horgan et al., 2020; Rampe et al., 2020).

Conversely, the Fe²⁺ ions mobilized by the reducing fluids from the gray outcrops would be able to move toward the interface with Ca-SO₄ fluids following redox potential gradients (Chan et al., 2005; e.g., 2004). Indeed, since sulfate ions (SO₄²⁻) are oxidizing agents (Barnes, 1997), the Ca-SO₄ bearing diagenetic fluids presented more oxidizing conditions compared to the surrounding host rock. Iron leached as Fe²⁺ from the adjacent host rock oxidized to Fe³⁺ and precipitated as gray crystalline hematite along with Ca-sulfate, in the form of substitution pseudomorphs to the gypsum-habit light-toned crystals (Figure 12, Panel 3A) (e.g., Lougheed, 1983; Warren, 2016) and hexagonal crystals and partial fills in light-toned Ca-sulfate veins (Figure 12, Panel 3B). In addition, the dissolution of hematite in the host rock could have been accelerated by the presence of SO₄-ions in the diagenetic fluids, as it would lead to an increased solubility of Fe³⁺ through the formation of comparably stable Fe³⁺-SO₄ complexes (Barnes, 1997).

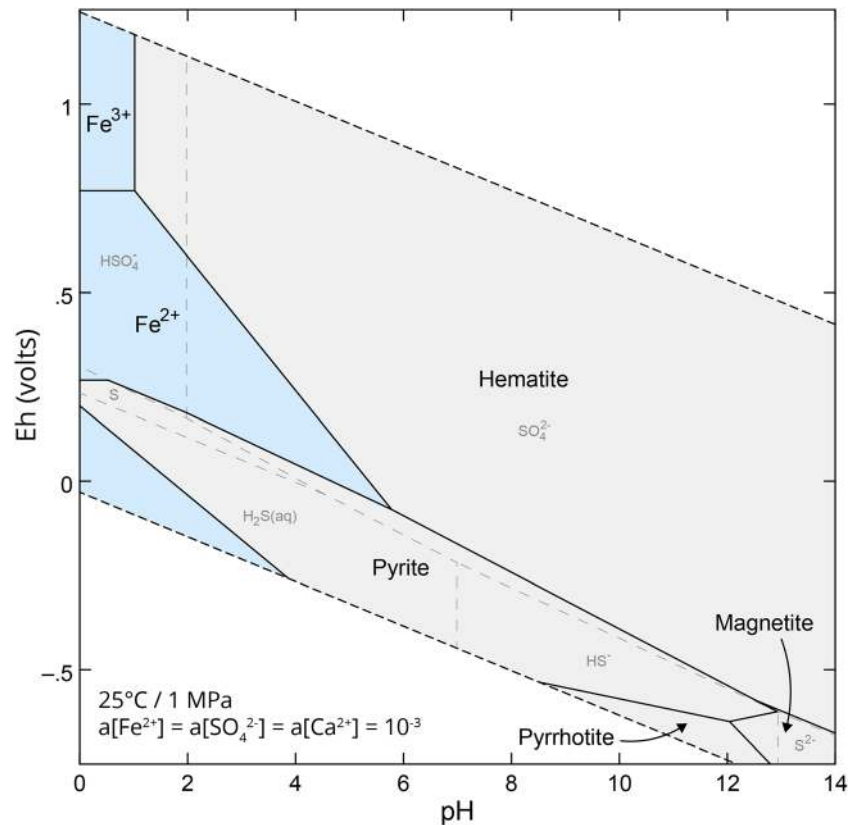


Figure 13. Eh-pH diagram for the Fe-S-Ca system, illustrating the thermodynamical stability fields of Fe-species (S species are indicated in light-gray). In this system, hematite constitutes the predominant phase except in reducing conditions, where pyrite is predicted to form, as well as pyrrhotite and magnetite in alkaline conditions. The stability diagram was calculated using Geochemical Workbench and the LNLL thermodynamical database (Delany & Lundeen, 1990). The activity for all elements is fixed arbitrarily at 10^{-2} .

The formation of hematite is also consistent with thermodynamic predictions, as illustrated by the Eh-pH diagram for the Fe-Ca-S system (Figure 13). Indeed, in this configuration, hematite is the most stable Fe-bearing phase over a broad range of pH and Eh conditions, except for reducing conditions where pyrite or pyrrhotite are expected to form instead (but neither are observed). In addition, laboratory experiments have shown that the presence of Ca²⁺ ions in solution enhanced the crystallization of hematite (Mohapatra et al., 2012). In contrast, the formation of magnetite appears to be unlikely, as it would require extremely alkaline and reducing fluid conditions.

5.3. Comparison With Previous Observations on Mars

The red-to-gray color gradients observed in the outcrops on VRR bear similarities with the outcrops of the Burns sedimentary formation, explored by the *Opportunity* rover at Meridiani Planum. While it consists of evaporitic sandstones that formed in transient eolian and shallow water conditions (Grotzinger et al., 2005; Squyres, 2004), the Burns formation outcrops also appear to have experienced an extended history of diagenetic alteration consistent with burial and periodic groundwater flow(s) (McLennan et al., 2005). There, syn-depositional and early-diagenetic intrasedimentary evaporite crystal molds are observed, followed by at least two distinct episodes of cementation associated with interstitial pore-water and groundwater recharge(s) as well as the formation of hematite “blueberry” concretions (Hurowitz et al., 2010; McLennan et al., 2005; Squyres & Knoll, 2005). However, the diagenetic Fe-oxide features observed at VRR display distinct morphologies with euhedral crystals, local pseudomorphs, and more complex polygonal shapes, compared to the well-rounded “blueberry” concretions observed at Meridiani, and as such originated from relatively different diagenetic processes. While hematite diagenetic features are only observed locally on VRR, and frequently in association with Ca-sulfate veins, the hematite concretions are

pervasive throughout the outcrops at Meridiani Planum. One major difference resides in the fact that the sedimentary rocks of the Burns formation at Meridiani Planum incorporate significantly more sulfate (up to 40 wt.%), including Fe-sulfates such as jarosite and possibly melanterite (Grotzinger et al., 2005; Squyres, 2004). As such, the mobility of Fe during diagenesis there was due to interaction with strongly acidic groundwater fluids (McLennan et al., 2005; Tosca & McLennan, 2006). Although acidic fluids may have been involved in the formation of the VRR rocks on account of the jarosite observed at least locally at the Rock Hall drill hole, the predominance of Ca-sulfate over other sulfur-rich phases does not favor strongly acidic systems, and the detrital nature of the VRR sedimentary rocks (mudstones and fine-grained sandstones) make them significantly distinct from Meridiani Planum.

Earth analog studies have been conducted in order to provide insights into the diagenetic processes that occurred at Meridiani Planum, especially regarding the formation of hematite concretions. Among them, the extensive study of the Jurassic Navajo Sandstones (Beitler et al., 2005; Chan et al., 2000, 2004, 2005, 2007; Ormö et al., 2004; Parry et al., 2009) is particularly relevant to VRR. Indeed, outcrops there exhibit lateral color variations associated with the syn-sedimentary to early-diagenetic red hematite formation in oxidizing conditions and subsequent diagenetic alteration by reducing fluids, bleaching the outcrops white-gray at millimeter to regional scales (Chan et al., 2004, 2005; Parry et al., 2009). Fe is either leached at that stage, incorporated into diagenetic fluids as Fe^{2+} and later forming hematite concretions upon encountering oxidizing fluids (Chan et al., 2005), or immediately fixed in ferroan dolomite, pyrite, and large crystallites of gray hematite (Parry et al., 2009). Similar processes could also account for the lateral color variations observed on top of VRR, with the early-diagenesis formation of ferric species (hematite, akaganeite, and jarosite) in oxidizing conditions and their subsequent alteration by groundwater fluids, probably reducing, leading to the coarsening of hematite grains through dissolution/recrystallization processes and Ostwald ripening (David et al., 2020; Horgan et al., 2020, and references therein).

Thus, with VRR and Meridiani Planum, the mobility of Fe during diagenesis has been observed in situ at two locations on Mars, likely resulting from the interaction of groundwater fluids in two distinct settings, both involving hematite but also metastable Fe-bearing species such as Fe-sulfate (e.g., jarosite) and Fe-oxide/hydroxide (e.g., akaganeite). As such, orbital detections of akaganeite in evaporitic basins at Antoniadi and Robert Sharp (in addition to Gale) (Buz et al., 2017; Carter et al., 2015) and detections of jarosite in Valles Marineris (Milliken et al., 2008), Noctis Labyrinthus (Thollot et al., 2012), within the vicinity of Mawrth Vallis (Farrand et al., 2009), and in the potential groundwater-fed paleolake deposits of Columbus crater at Terra Sirenum (Wray et al., 2011) could constitute areas of interest for investigating groundwater interactions and the mobility of Fe during diagenesis on Mars. Orbital studies suggest that the diagenetic processes observed at VRR may be relatively frequent on Mars, and our results show that the Meridiani Planum case should not be taken as the unique ground truth of such diagenetic systems.

6. Conclusion

The in situ exploration of VRR by the rover *Curiosity* has revealed a complex postdepositional geological history (Figure 12). The lateral color patterns observed in the VRR outcrops are attributed to syn-depositional or early diagenetic formation of ferric species (red color), and subsequent alteration by groundwater (to gray color). Within the gray outcrops, ChemCam highlighted that iron was locally mobilized from the host rock, likely by reducing groundwater fluids during diagenesis (as Fe^{2+}), to form ferric (Fe^{3+}) oxide as pseudomorphs of euhedral gypsum crystals, through the coarsening of preexisting Fe-oxides in the host rock, and as hexagonal crystalline inclusions and partial vein fills within late-diagenetic Ca-sulfate fracture-fills. In the process, Fe was leached from the adjacent host rock upon interaction with SO_4^{2-} bearing fluids, forming low-Fe bleached halos around the Fe-oxide diagenetic features. The formation of these diagenetic Fe-oxide minerals, interpreted as coarse-grained crystalline hematite, highlights the complex redox-driven processes that occurred during diagenesis and the induced mobility of redox-sensitive elements (mainly Fe, but also Mn to a lesser extent) occurring well after deposition and sedimentation. Thus, millimeter-scale observations from ChemCam show that diagenetic processes likely played a significant role in the formation of VRR, a topographic structure visible from orbit.

References

- Abramoff, M. D., Magalhães, P. J., & Ram, S. J. (2004). Image processing with ImageJ. *Biophotonics International*, 11, 36–42.
- Anderson, R. (2010). Geologic mapping and characterization of Gale Crater and implications for its potential as a Mars Science Laboratory landing site. *The Mars Journal*, 5, 76–128. <https://doi.org/10.1555/mars.2010.0004>
- Anderson, R. B., Clegg, S. M., Frydenvang, J., Wiens, R. C., McLennan, S., Morris, R. V., et al. (2017). Improved accuracy in quantitative laser-induced breakdown spectroscopy using sub-models. *Spectrochim. Acta Part B At. Spectrosc.*, 129, 49–57. <https://doi.org/10.1016/j.sab.2016.12.002>
- Bain, R. J. (1990). Diagenetic, nonevaporative origin for gypsum. *Geology*, 18, 447. [https://doi.org/10.1130/0091-7613\(1990\)018<0447: DNOFG>2.3.CO;2](https://doi.org/10.1130/0091-7613(1990)018<0447: DNOFG>2.3.CO;2)
- Banham, S. G., Gupta, S., Rubin, D. M., Watkins, J. A., Sumner, D. Y., Edgett, K. S., et al. (2018). Ancient Martian aeolian processes and palaeomorphology reconstructed from the Stimson formation on the lower slope of Aeolis Mons, Gale crater, Mars. *Sedimentology*, 65, 993–1042. <https://doi.org/10.1111/sed.12469>
- Barnes, H. L. (1997). *Geochemistry of hydrothermal ore deposits* (3rd ed.). New Jersey, USA: John Wiley & Sons.
- Baron, F., Gaudin, A., Lorand, J. -P., & Mangold, N. (2019). New constraints on early Mars weathering conditions from an experimental approach on crust simulants. *Journal of Geophysical Research: Planets*, 124, 1783–1801. <https://doi.org/10.1029/2019JE005920>
- Beitler, B., Parry, W. T., & Chan, M. A. (2005). Fingerprints of fluid flow: Chemical diagenetic history of the Jurassic Navajo Sandstone, Southern Utah, U.S.A. *Journal of Sedimentary Research*, 75, 547–561. <https://doi.org/10.2110/jsr.2005.045>
- Bennett, K. A., Rivera-Hernandez, F., Tinker, C., Horgan, B., Fey, D. M., Edwards, C., et al. (2020). Extensive diagenesis revealed by fine-scale features at Vera Rubin ridge, Gale crater, Mars. *Journal of Geophysical Research: Planets*.
- Buz, J., Ehlmann, B. L., Pan, L., & Grotzinger, J. P. (2017). Mineralogy and stratigraphy of the Gale crater rim, wall, and floor units. *Journal of Geophysical Research: Planets*, 122, 1090–1118. <https://doi.org/10.1002/2016JE005163>
- Carter, J., Viviano-Beck, C., Loizeau, D., Bishop, J., & Le Deit, L. (2015). Orbital detection and implications of akaganéite on Mars. *Icarus*, 253, 296–310. <https://doi.org/10.1016/j.icarus.2015.01.020>
- Caswell, T. E., & Milliken, R. E. (2017). Evidence for hydraulic fracturing at Gale crater, Mars: Implications for burial depth of the Yellowknife Bay formation. *Earth and Planetary Science Letters*, 468, 72–84. <https://doi.org/10.1016/j.epsl.2017.03.033>
- Chan, M. A., Beitler, B., Parry, W. T., Örmö, J., & Komatsu, G. (2004). A possible terrestrial analogue for haematite concretions on Mars. *Nature*, 429, 731–734. <https://doi.org/10.1038/nature02600>
- Chan, M. A., Bowen, B. B., Parry, W. T., Örmö, J., & Komatsu, G. (2005). Red rock and red planet diagenesis: Comparisons of Earth and Mars concretions. *GSA Today*, 15, 4–10. [https://doi.org/10.1130/1052-5173\(2005\)15<4:TEOTDI>2.0.CO;2](https://doi.org/10.1130/1052-5173(2005)15<4:TEOTDI>2.0.CO;2)
- Chan, M. A., Örmö, J., Park, A. J., Stich, M., Souza-Egipsy, V., & Komatsu, G. (2007). Models of iron oxide concretion formation: Field, numerical, and laboratory comparisons. *Geofluids*, 7, 356–368. <https://doi.org/10.1111/j.1468-8123.2007.00187.x>
- Chan, M. A., Parry, W. T., & Bownman, J. R. (2000). Diagenetic hematite and manganese oxides and fault-related fluid flow in Jurassic Sandstones, Southeastern Utah. *American Association of Petroleum Geologists Bulletin*, 84, 1281–1310. <https://doi.org/10.1306/A9673E82-1738-11D7-8645000102C1865D>
- Clegg, S. M., Anderson, R. B., Rapin, W., Ehlmann, B. L., Anderson, D. E., Thomas, N. H., et al. (2018). ChemCam sulfur quantitative analysis and interpretation. In *49th Lunar and Planetary Science Conference*.
- Clegg, S. M., Wiens, R. C., Anderson, R., Forni, O., Frydenvang, J., Lasue, J., et al. (2017). Recalibration of the Mars Science Laboratory ChemCam instrument with an expanded geochemical database. *Spectrochim. Acta Part B At. Spectrosc.*, 129, 64–85. <https://doi.org/10.1016/j.sab.2016.12.003>
- Cornell, R. M., & Schwertmann, U. (2003). *The iron oxides, techniques*. KGaA, Weinheim, FRG: Wiley-VCH Verlag GmbH & Co. <https://doi.org/10.1002/3527602097>
- David, G., Cousin, A., Forni, O., Meslin, P. -Y., Dehouck, E., Mangold, N., et al. (2020). Analyses of high-iron sedimentary bedrock and diagenetic features observed with ChemCam at Vera Rubin ridge, Gale crater, Mars: calibration and characterization. *Journal of Geophysical Research: Planets*, 125, e2019JE006314. <https://doi.org/10.1029/2019JE006314>
- De Toffoli, B., Mangold, N., Massironi, M., Zanella, A., Pozzobon, R., le Mouélic, S., et al. (2020). Structural analysis of sulfate vein networks in Gale crater (Mars). *Journal of Structural Geology*, 137, 104083. <https://doi.org/10.1016/j.jsg.2020.104083>
- Dehouck, E., Gaudin, A., Chevrier, V., & Mangold, N. (2016). Mineralogical record of the redox conditions on early Mars. *Icarus*, 271, 67–75. <https://doi.org/10.1016/j.icarus.2016.01.030>
- Delany, J. M., & Lundeen, S. R. (1990). *The LLNL thermodynamic database. Lawrence Livermore Natl. Lab. Rep. UCRL-21658*. Livermore, California, USA: Lawrence Livermore Natl. Lab.
- Edgar, L. A., Fedo, C. M., Gupta, S., Banham, S. G., Fraeman, A. A., Grotzinger, J. P., et al. (2020). A Lacustrine Paleoenvironment Recorded at Vera RubinRidge, Gale Crater: Overview of the Sedimentology and Stratigraphy Observed by the Mars ScienceLaboratory Curiosity Rover. *Journal of Geophysical Research: Planets*, 125, e2019JE006307. <https://doi.org/10.1029/2019JE006307>
- Edgett, K. S., Yingt, R. A., Ravine, M. A., Caplinger, M. A., Maki, J. N., Ghaemi, F. T., et al. (2012). Curiosity's Mars Hand Lens Imager (MAHLI) investigation. *Space Science Reviews*, 170, 259–317. <https://doi.org/10.1007/s11214-012-9910-4>
- El-Tabakh, M., Riccioni, R., & Schreiber, B. (1997). Evolution of late Triassic rift basin evaporites (Passaic Formation): Newark Basin, Eastern North America. *Sedimentology*, 44, 767–790. <https://doi.org/10.1046/j.1365-3091.1997.d01-47.x>
- Farrand, W. H., Glotch, T. D., Rice, J. W., Hurovitz, J. A., & Swayze, G. A. (2009). Discovery of jarosite within the Mawrth Vallis region of Mars: Implications for the geologic history of the region. *Icarus*. <https://doi.org/10.1016/j.icarus.2009.07.014>
- Fedo, C. M., Grotzinger, J. P., Gupta, S., Fraeman, A., Edgar, L., Edgett, K., et al. (2018). Sedimentology and stratigraphy of the Murray Formation, Gale Crater, Mars. In *49th Lunar and Planetary Science Conference*.
- Forni, O., Gaft, M., Toplis, M. J., Clegg, S. M., Maurice, S., Wiens, R. C., et al. (2015). First detection of fluorine on Mars: Implications for Gale Crater's geochemistry. *Geophysical Research Letters*, 42, 1020–1028. <https://doi.org/10.1002/2014GL02742>
- Fraeman, A. A., Arvidson, R. E., Catalano, J. G., Grotzinger, J. P., Morris, R. V., Murchie, S. L., et al. (2013). A hematite-bearing layer in Gale Crater, Mars: Mapping and implications for past aqueous conditions. *Geology*, 41, 1103–1106. <https://doi.org/10.1130/G34613.1>
- Fraeman, A. A., Arvidson, R. E., Horgan, B. H., Jacob, S. R., Johnson, J. R., Morris, R. V., et al. (2019). Synergistic orbital and in situ observations at Vera Rubin Ridge: Comparing CRISM and Curiosity Observations. In *50th Lunar and Planetary Science Conference*.
- Fraeman, A. A., Edgar, L. A., Grotzinger, J. P., Vasavada, A. R., Johnson, J. R., Wellington, D. F., et al. (2018). Curiosity's investigation at Vera Rubin ridge. In *49th Lunar and Planetary Science Conference*.

Acknowledgments

We are indebted to the Mars Science Laboratory Project engineering and science teams for their participations in tactical and strategic operations. All data used in this study are accessible at the Planetary Data System (<http://pds-geosciences.wustl.edu/missions/msl/index.htm>). Data provided by the ChemCam instrument are supported in the United States by NASA's Mars Exploration Program and in France by the Centre National d'Etudes Spatiales (CNES) and the Agence Nationale de la Recherche (ANR) under the program ANR-16-CE31-0012 entitled "Mars-Prime." J. Frydenvang acknowledges the support of the Carlsberg Foundation.

- Fraeman, A. A., Edgar, L. A., Rampe, E. B., Thompson, L. M., Frydenvang, J., Fedo, C. M., et al. (2020). Evidence for a diagenetic origin of Vera Rubin ridge, Gale Crater, Mars: Summary and synthesis of Curiosity's exploration campaign. *Journal of Geophysical Research: Planets*, *125*, e2020JE006527. <https://doi.org/10.1029/2020JE006527>
- Fraeman, A. A., Ehlmann, B. L., Arvidson, R. E., Edwards, C. S., Grotzinger, J. P., Milliken, R. E., et al. (2016). The stratigraphy and evolution of lower Mount Sharp from spectral, morphological, and thermophysical orbital data sets. *Journal of Geophysical Research: Planets*, *121*, 1713–1736. <https://doi.org/10.1002/2016JE005095>
- Frydenvang, J., Gasda, P. J., Hurowitz, J. A., Grotzinger, J. P., Wiens, R. C., Newsom, H. E., et al. (2017). Diagenetic silica enrichment and late-stage groundwater activity in Gale crater, Mars. *Geophysical Research Letters*, *44*, 4716–4724. <https://doi.org/10.1002/2017GL073323>
- Frydenvang, J., Mangold, N., Wiens, R. C., Fraeman, A. A., Edgar, L. A., Fedo, C., et al. (2020). The chemostratigraphy of the Murray formation and role of diagenesis at Vera Rubin ridge in Gale crater, Mars, as observed by the ChemCam instrument. *Journal of Geophysical Research: Planets*, *125*, e2019JE006320. <https://doi.org/10.1029/2019JE006320>
- Gasda, P. J., Haldeman, E. B., Wiens, R. C., Rapin, W., Bristow, T. F., Bridges, J. C., et al. (2017). In situ detection of boron by ChemCam on Mars. *Geophysical Research Letters*, *44*, 8739–8748. <https://doi.org/10.1002/2017GL074480>
- Grotzinger, J. P., Arvidson, R. E., Bell, J. F., Calvin, W., Clark, B. C., Fike, D. A., et al. (2005). Stratigraphy and sedimentology of a dry to wet eolian depositional system, Burns formation, Meridiani Planum, Mars. *Earth and Planetary Science Letters*, *240*, 11–72. <https://doi.org/10.1016/j.epsl.2005.09.039>
- Grotzinger, J. P., Crisp, J., Vasavada, A. R., Anderson, R. C., Baker, C. J., Barry, R., et al. (2012). Mars Science Laboratory mission and science investigation. *Space Science Reviews*. <https://doi.org/10.1007/s11214-012-9892-2>
- Grotzinger, J. P., Gupta, S., Malin, M. C., Rubin, D. M., Schieber, J., Siebach, K., et al. (2015). Deposition, exhumation, and paleoclimate of an ancient lake deposit, Gale crater, Mars. *Science (80-)*, *350*, aac7575–aac7575. <https://doi.org/10.1126/science.aac7575>
- Grotzinger, J. P., Sumner, D. Y., Kah, L. C., Stack, K., Gupta, S., Edgar, L., et al. (2014). A habitable fluvio-lacustrine environment at Yellowknife Bay, Gale Crater, Mars. *Science (80-)*, *343*, 1242777. <https://doi.org/10.1126/science.1242777>
- Hardie, L. (1985). The problem of distinguishing between primary and secondary features in evaporites. In *Sixth Int. Symp. salt* (Vol. 1, pp. 173–195). Alexandria, Virginia, USA: Salt Institute.
- Herd, C. D. K., Borg, L. E., Jones, J. H., & Papike, J. J. (2002). Oxygen fugacity and geochemical variations in the martian basalts: Implications for martian basalt petrogenesis and the oxidation state of the upper mantle of Mars. *Geochimica et Cosmochimica Acta*, *66*, 2025–2036. [https://doi.org/10.1016/S0016-7037\(02\)00828-1](https://doi.org/10.1016/S0016-7037(02)00828-1)
- Horgan, B., Johnson, J. R., Fraeman, A. A., Rice, M. S., Seeger, C., Bell, J. F., et al. (2020). Diagenesis of Vera Rubin ridge, Gale crater, Mars from Mastcam multispectral images. *Journal of Geophysical Research: Planets*, e2019JE006322.
- Hurowitz, J. A., Fischer, W. W., Tosca, N. J., & Milliken, R. E. (2010). Origin of acidic surface waters and the evolution of atmospheric chemistry on early Mars. *Nature Geoscience*, *3*, 323–326. <https://doi.org/10.1038/ngeo831>
- Hurowitz, J. A., Grotzinger, J. P., Fischer, W. W., McLennan, S. M., Milliken, R. E., Stein, N., et al. (2017). Redox stratification of an ancient lake in Gale crater, Mars. *Science (80-)*, *356*, eaah6849. <https://doi.org/10.1126/science.aah6849>
- Jacob, S. R., Wellington, D. F., Bell, J. F. III, Achilles, C., Fraeman, A. A., Horgan, B., et al. (2020). Spectral, compositional, and physical properties of the upper murray formation and Vera Rubin ridge, Gale Crater, Mars. *Journal of Geophysical Research: Planets*, *125*, e2019JE006290. <https://doi.org/10.1029/2019JE006290>
- Johnson, J. R., Achilles, C. N., Bell, J. F., Bender, S., Cloutis, E., Ehlmann, B., et al. (2017). Visible/near-infrared spectral diversity from in situ observations of the Bagnold Dune Field sands in Gale Crater, Mars. *Journal of Geophysical Research: Planets*. <https://doi.org/10.1002/2016JE005187>
- Johnson, J. R., Bell, J. F., Bender, S., Blaney, D., Cloutis, E., DeFlores, L., et al. (2015). ChemCam passive reflectance spectroscopy of surface materials at the Curiosity landing site, Mars. *Icarus*, *249*, 74–92. <https://doi.org/10.1016/j.icarus.2014.02.028>
- Johnson, J. R., Bell, J. F., Bender, S., Blaney, D., Cloutis, E., Ehlmann, B., et al. (2016). Constraints on iron sulfate and iron oxide mineralogy from ChemCam visible/near-infrared reflectance spectroscopy of Mt. Sharp basal units, Gale Crater, Mars. *American Mineralogist*, *101*, 1501–1514. <https://doi.org/10.2138/am-2016-5553>
- Kah, L. C., Stack, K. M., Eigenbrode, J. L., Yingst, R. A., & Edgett, K. S. (2018). Syndepositional precipitation of calcium sulfate in Gale Crater, Mars. *Terra Nova*, *30*, 431–439. <https://doi.org/10.1111/ter.12359>
- Kronyak, R. E., Kah, L. C., Edgett, K. S., VanBommel, S. J., Thompson, L. M., Wiens, R. C., et al. (2019). Mineral-filled fractures as indicators of multigenerational fluid flow in the Pahrump Hills Member of the Murray Formation, Gale Crater, Mars. *Earth and Space Science*, *6*, 238–265. <https://doi.org/10.1029/2018EA000482>
- L'Haridon, J., Mangold, N., Meslin, P.-Y. Y., Johnson, J. R., Rapin, W., Forni, O., et al. (2018). Chemical variability in mineralized veins observed by ChemCam on the lower slopes of Mount Sharp in Gale crater, Mars. *Icarus*, *311*, 69–86. <https://doi.org/10.1016/j.icarus.2018.01.028>
- Lane, M. D., Morris, R. V., Mertzman, S. A., & Christensen, P. R. (2002). Evidence for platy hematite grains in Sinus Meridiani, Mars. *Journal of Geophysical Research*, *107*, 9-1–9-15. <https://doi.org/10.1029/2001JE001832>
- Lanza, N. L., Fischer, W. W., Wiens, R. C., Grotzinger, J., Ollila, A. M., Cousin, A., et al. (2014). High manganese concentrations in rocks at Gale crater, Mars. *Geophysical Research Letters*, *41*, 5755–5763. <https://doi.org/10.1002/2014GL060329>
- Lasue, J., Clegg, S. M., Forni, O., Cousin, A., Wiens, R. C., Lanza, N., et al. (2016). Observation of >5 wt % zinc at the Kimberley outcrop, Gale crater, Mars. *Journal of Geophysical Research: Planets*, *121*, 338–352. <https://doi.org/10.1002/2015JE004946>
- Le Mouélic, S., Gasnault, O., Herkenhoff, K. E., Bridges, N. T., Langevin, Y., Mangold, N., et al. (2015). The ChemCam Remote Micro-Imager at Gale crater: Review of the first year of operations on Mars. *Icarus*, *249*, 93–107. <https://doi.org/10.1016/j.icarus.2014.05.030>
- Lougheed, M. S. (1983). Origin of Precambrian iron-formations in the Lake Superior region. *Geological Society of America Bulletin*, *94*, 325. [https://doi.org/10.1130/0016-7606\(1983\)94<325:OOPIIT>2.0.CO;2](https://doi.org/10.1130/0016-7606(1983)94<325:OOPIIT>2.0.CO;2)
- Malin, M. C., Ravine, M. A., Caplinger, M. A., Tony Ghaemi, F., Schaffner, J. A., Maki, J. N., et al. (2017). The Mars Science Laboratory (MSL) Mast cameras and Descent imager: Investigation and instrument descriptions. *Earth and Space Science*, *4*, 506–539. <https://doi.org/10.1002/2016EA000252>
- Maurice, S., Clegg, S. M., Wiens, R. C., Gasnault, O., Rapin, W., Forni, O., et al. (2016). ChemCam activities and discoveries during the nominal mission of the Mars Science Laboratory in Gale crater, Mars. *Journal of Analytical Atomic Spectrometry*, *31*, 863–889. <https://doi.org/10.1039/C5JA00417A>
- Maurice, S., Wiens, R. C., Saccoccio, M., Barraclough, B., Gasnault, O., Forni, O., et al. (2012). The ChemCam Instrument Suite on the Mars Science Laboratory (MSL) Rover: Science objectives and mast unit description. *Space Science Reviews*, *170*, 95–166. <https://doi.org/10.1007/s11214-012-9912-2>

- McLennan, S. M., Bell, J. F., Calvin, W. M., Christensen, P. R., Clark, B. C., de Souza, P. A., et al. (2005). Provenance and diagenesis of the evaporite-bearing Burns formation, Meridiani Planum, Mars. *Earth and Planetary Science Letters*, *240*, 95–121. <https://doi.org/10.1016/j.epsl.2005.09.041>
- Meslin, P.-Y., Cicutto, L., Forni, O., Drouet, C., Rapin, W., Nachon, M., et al. (2016). Calibration of the Fluorine, Chlorine, and Hydrogen Content of Apatites with the ChemCam LIBS Instrument. In *47th Lunar and Planetary Science Conference*.
- Meslin, P.-Y., Gasda, P., L'Haridon, J., Forni, O., Lanza, N., Lamm, S., et al. (2018). Detection of hydrous manganese and iron oxides with variable phosphorus and magnesium contents in the lacustrine sediments of the Murray Formation, Gale, Mars. In *49th Lunar and Planetary Science Conference*.
- Milliken, R. E., Grotzinger, J. P., & Thomson, B. J. (2010). Paleoclimate of Mars as captured by the stratigraphic record in Gale Crater. *Geophysical Research Letters*, *37*, 1238670. <https://doi.org/10.1029/2009GL041870>
- Milliken, R. E., Swayze, G. A., Arvidson, R. E., Bishop, J. L., Clark, R. N., Ehlmann, B. L., et al. (2008). Opaline silica in young deposits on Mars. *Geology*. <https://doi.org/10.1130/G24967A.1>
- Mohapatra, M., Behera, D., Layek, S., Anand, S., Verma, H. C., & Mishra, B. K. (2012). Influence of Ca ions on surfactant directed nucleation and growth of nano structured iron oxides and their magnetic properties. *Crystal Growth & Design*, *12*, 18–28. <https://doi.org/10.1021/cg201124c>
- Morris, R. V., Lauer, H. V., Lawson, C. A., Gibson, E. K., Nace, G. A., & Stewart, C. (1985). Spectral and other physicochemical properties of submicron powders of hematite (α -Fe₂O₃), maghemite (γ -Fe₂O₃), magnetite (Fe₃O₄), goethite (α -FeOOH), and lepidocrocite (γ -FeOOH). *Journal of Geophysical Research*, *90*, 3126. <https://doi.org/10.1029/JB090iB04p03126>
- Murray, R. C. (1964). Origin and diagenesis of gypsum and anhydrite. *SEPM: Society for Sedimentary Geology*, *34*, 512–523. <https://doi.org/10.1306/74D710D2-2B21-11D7-8648000102C1865D>
- Nachon, M., Clegg, S. M., Mangold, N., Schröder, S., Kah, L. C., Dromart, G., et al. (2014). Calcium sulfate veins characterized by ChemCam/Curiosity at Gale crater, Mars. *Journal of Geophysical Research: Planets*, *119*, 1991–2016. <https://doi.org/10.1002/2013JE004588>
- Nachon, M., Mangold, N., Forni, O., Kah, L. C., Cousin, A., Wiens, R. C., et al. (2016). Chemistry of diagenetic features analyzed by ChemCam at Pahrump Hills, Gale crater, Mars. *Icarus*, *0*, 1–16. <https://doi.org/10.1016/j.icarus.2016.08.026>
- Nachon, M., Sumner, D. Y., Borges, S. R., Stack, K., Stein, N., Watkins, J. A., et al. (2017). Stratigraphic distribution of veins in the Murray and Stimson formations, Gale crater, Mars: Implications for ancient groundwater circulation. In *AGU Fall Meet.*
- Ormö, J., Komatsu, G., Chan, M. A., Beitler, B., & Parry, W. T. (2004). Geological features indicative of processes related to the hematite formation in Meridiani Planum and Aram Chaos, Mars: A comparison with diagenetic hematite deposits in southern Utah, USA. *Icarus*, *171*, 295–316. <https://doi.org/10.1016/j.icarus.2004.06.001>
- Paik, I. S., Huh, M., So, Y. H., Lee, J. E., & Kim, H. J. (2007). Traces of evaporites in Upper Cretaceous lacustrine deposits of Korea: Origin and paleoenvironmental implications. *Journal of Asian Earth Sciences*, *30*, 93–107. <https://doi.org/10.1016/j.jseaes.2006.07.013>
- Parry, W. T., Chan, M. A., & Nash, B. P. (2009). Diagenetic characteristics of the Jurassic Navajo Sandstone in the Covenant oil field, central Utah thrust belt. *American Association of Petroleum Geologists Bulletin*, *93*, 1039–1061. <https://doi.org/10.1306/04270908170>
- Payré, V., Fabre, C., Cousin, A., Sautter, V., Wiens, R. C., Forni, O., et al. (2017). Alkali trace elements in Gale crater, Mars, with ChemCam: Calibration update and geological implications. *Journal of Geophysical Research: Planets*, *119*, 1276–1301. <https://doi.org/10.1002/2016JE005201>
- Payré, V., Fabre, C., Sautter, V., Cousin, A., Mangold, N., Deit, L. L., et al. (2019). Copper enrichments in the Kimberley formation in Gale crater, Mars: Evidence for a Cu deposit at the source. *Icarus*, *321*, 736–751. <https://doi.org/10.1016/j.icarus.2018.12.015>
- Post, J. E. (1999). Manganese oxide minerals: Crystal structures and economic and environmental significance. *Proceedings of the National Academy of Sciences*. <https://doi.org/10.1073/pnas.96.7.3447>
- Rampe, E. B., Bristow, T. F., Morris, R. V., Morrison, S. M., Achilles, C. N., Ming, D. W., et al. (2020). Mineralogy of Vera Rubin Ridge from the Mars Science Laboratory CheMin Instrument. *Journal of Geophysical Research: Planets*, *125*, e2019JE006306. <https://doi.org/10.1029/2019JE006306>
- Rapin, W., Ehlmann, B. L., Dromart, G., Schieber, J., Thomas, N. H., Fischer, W. W., et al. (2019). An interval of high salinity in ancient Gale crater lake on Mars. *Nature Geoscience*, *12*, 889–895. <https://doi.org/10.1038/s41561-019-0458-8>
- Rapin, W., Meslin, P.-Y., Maurice, S., Vaniman, D., Nachon, M., Mangold, N., et al. (2016). Hydration state of calcium sulfates in Gale crater, Mars: Identification of bassanite veins. *Earth and Planetary Science Letters*, *452*, 197–205. <https://doi.org/10.1016/j.epsl.2016.07.045>
- Rapin, W., Meslin, P.-Y., Maurice, S., Wiens, R. C., Laporte, D., Chauviré, B., et al. (2017). Quantification of water content by laser induced breakdown spectroscopy on Mars. *Spectrochimica Acta Part B: Atomic Spectroscopy*, *130*, 82–100. <https://doi.org/10.1016/j.sab.2017.02.007>
- Schindelin, J., Arganda-Carreras, I., Frise, E., Kaynig, V., Longair, M., Pietzsch, T., et al. (2012). Fiji: An open-source platform for biological-image analysis. *Nature Methods*, *9*, 676. <https://doi.org/10.1038/nmeth.2019>
- Schwenzer, S. P., Bridges, J. C., Wiens, R. C., Conrad, P. G., Kelley, S. P., Leveille, R., et al. (2016). Fluids during diagenesis and sulfate vein formation in sediments at Gale crater, Mars. *Meteoritics and Planetary Science*, *28*. <https://doi.org/10.1111/maps.12668>
- Squyres, S. W. (2004). In situ evidence for an ancient aqueous environment at Meridiani Planum, Mars. *Science (80-)*, *306*, 1709–1714. <https://doi.org/10.1126/science.1104559>
- Squyres, S. W., & Knoll, A. H. (2005). Sedimentary rocks at Meridiani Planum: Origin, diagenesis, and implications for life on Mars. *Earth and Planetary Science Letters*. <https://doi.org/10.1016/j.epsl.2005.09.038>
- Sugimoto, T., Muramatsu, A., Sakata, K., & Shindo, D. (1993). Characterization of hematite particles of different shapes. *Journal of Colloid and Interface Science*, *158*, 420–428. <https://doi.org/10.1006/jcis.1993.1274>
- Sugimoto, T., Waki, S., Itoh, H., & Muramatsu, A. (1996). Preparation of monodisperse platelet-type hematite particles from a highly condensed β -FeOOH suspension. *Colloids and Surfaces A: Physicochemical and Engineering Aspects*, *109*, 155–165. [https://doi.org/10.1016/0927-7757\(95\)03454-4](https://doi.org/10.1016/0927-7757(95)03454-4)
- Thollot, P., Mangold, N., Ansan, V., Le Mouélic, S., Milliken, R. E., Bishop, J. L., et al. (2012). Most Mars minerals in a nutshell: Various alteration phases formed in a single environment in Noctis Labyrinthus. *Journal of Geophysical Research*, *117*, n/a–n/a. <https://doi.org/10.1029/2011JE004028>
- Thomas, N. H., Ehlmann, B. L., Meslin, P.-Y., Cousin, A., Forni, O., Rapin, W., et al. (2018). MSL ChemCam observations of chloride salts in Gale Crater, Mars. In *49th Lunar and Planetary Science Conference*.

- Thompson, L. M., Berger, J. A., Spray, J. G., Fraeman, A. A., McCraig, M., O'Connell-Cooper, C., et al. (2020). APXS-derived compositional characteristics of Vera Rubin Ridge and Murray formation, Gale crater, Mars: Geochemical implications for the origin of the ridge. *Journal of Geophysical Research: Planets*.
- Tosca, N. J., & McLennan, S. M. (2006). Chemical divides and evaporite assemblages on Mars. *Earth and Planetary Science Letters*, *241*, 21–31. <https://doi.org/10.1016/j.epsl.2005.10.021>
- Vasavada, A. R., Grotzinger, J. P., Arvidson, R. E. E., Calef, F. J., Crisp, J. A., Gupta, S., et al. (2014). Overview of the Mars Science Laboratory mission: Bradbury Landing to Yellowknife Bay and beyond. *Journal of Geophysical Research: Planets*, *119*, 1134–1161. <https://doi.org/10.1002/2014JE004622>
- Warren, J. K. (2016). *Evaporites*. Cham: Springer International Publishing. <https://doi.org/10.1007/978-3-319-13512-0>
- Wiens, R. C., & Maurice, S. (2015). ChemCam: Chemostratigraphy by the First Mars Microprobe. *Elements*, *11*, 33–38. <https://doi.org/10.2113/gselements.11.1.33>
- Wiens, R. C., Maurice, S., Barraclough, B., Saccoccio, M., Barkley, W. C., Bell, J. F., et al. (2012). The ChemCam Instrument Suite on the Mars Science Laboratory (MSL) Rover: Body unit and combined system tests. *Space Science Reviews*, *170*, 167–227. <https://doi.org/10.1007/s11214-012-9902-4>
- Wong, G. M., Lewis, J. M. T., Knudson, C. A., Millan, M., McAdam, A. C., Eigenbrode, J. L., et al. (2020). Detection of reduced sulfur on Vera Rubin ridge by quadratic discriminant analysis of volatiles observed during evolved gas analysis. *Journal of Geophysical Research: Planets*. <https://doi.org/10.1029/2019JE006304>
- Wray, J. J., Milliken, R. E., Dundas, C. M., Swayze, G. A., Andrews-Hanna, J. C., Baldrige, A. M., et al. (2011). Columbus crater and other possible groundwater-fed paleolakes of Terra Sirenum, Mars. *Journal of Geophysical Research* *116*, E01001. <https://doi.org/10.1029/2010JE003694>